MULTISCALE MODEL. SIMUL.
Vol. 19, No. 3, pp. 1285–1309

© 2021 Society for Industrial and Applied Mathematics

Downloaded 08/22/21 to 130.215.63.230. Redistribution subject to SIAM license or copyright; see https://epubs.siam.org/page/terms

HIGH-FREQUENCY HOMOGENIZATION FOR ELECTROMAGNETIC HEATING OF PERIODIC MEDIA[*]

JOSEPH M. GAONE[†], BURT S. TILLEY[‡], AND VADIM V. YAKOVLEV[§]

Abstract. Electromagnetic heating is the process where a composite material absorbs applied electromagnetic radiation and converts this energy to internal energy in the material. While homogenization models for electromagnetic heating have been around for decades, these approaches break down when the wavelength of the electromagnetic wave is comparable to the characteristic microscale length. Here we derive from Maxwell's equations and the energy equation effective equations for a binary composite in the case where the characteristic microscale length and wavelength are comparable. Under the assumption of small loss factors in the materials, high-frequency homogenization results in a locally temperature dependent elliptic problem for the field amplitude via Floquet–Bloch theory. The length scale for thermal transport is the macroscale, and classical homogenization applies. We characterize the results in terms of a complex wavenumber for propagation, and validate our results for a lamellar structure for which an exact solution exists under isothermal conditions, and characterize field strength needed to achieve thermal runaway in the composite as a function of the resonant frequency and volume fraction of the lossless material.

Key words. mathematical modeling, microwave heating, heat exchanger, solar thermal collection, thermal runaway, photonic crystal

AMS subject classifications. 00A71, 35Q60, 80A20

DOI. 10.1137/20M1369415

1. Introduction.

Electromagnetic (EM) heating has been widely used in industrial applications including food processing [8, 42, 65, 50, 18, 12], microwave assisted chemistry [39, 21, 43] including chemical vapor infiltration [56, 25, 6, 5], and material processing [1, 15, 11, 53, 13, 7, 32, 61]. Many of these applications involve the heating of inhomogeneous media such as composites [25, 47, 38], ceramics [29, 40, 3, 46], and porous media [34, 37, 55, 31, 17]. The motivation of this work is to study the electromagnetic response to a porous EM heat exchanger, which converts EM radiation to thermal energy by fluid transport through a porous medium subject to dielectric heating. This study is performed through the application of homogenization theory.

Homogenization is a mathematical theory to model the macroscale behavior of a physical process through some well defined averaging process over the microscale structure. Homogenization in electromagnetics began with the development of mixture formula including the well known Maxwell–Garnett and Bruggemann formulas among others [51]. This approach attempts to find an appropriate averaging of the parameters of each constituent to determine an effective parameter that when applied

---

[*] Received by the editors September 25, 2020; accepted for publication (in revised form) May 10, 2021; published electronically August 12, 2021.
https://doi.org/10.1137/20M1369415

Funding: This work was funded by AFOSR awards FA9550-15-0476, FA9550-18-1-0528, and NSF MRI grant DMS-1337943 for high performance computing.

[†] The MITRE Corporation, Bedford, MA 01730-1420 USA (jgaone@mitre.org). 1. Approved for Public Release; Distribution Unlimited. Public Release Case Number 20-2558. 2. The author's affiliation with The MITRE Corporation is provided for identification purposes only, and is not intended to convey or imply MITRE's concurrence with, or support for, the positions, opinions, or viewpoints expressed by the author.

[‡] Corresponding author. Center for Industrial Mathematics and Statistics, Department of Mathematical Sciences, Worcester Polytechnic Institute, Worcester, MA 01609-2280 USA (tilley@wpi.edu).

[§] Center for Industrial Mathematics and Statistics, Department of Mathematical Sciences, Worcester Polytechnic Institute, Worcester, MA 01609-2280 USA (vadim@wpi.edu).

Copyright © by SIAM. Unauthorized reproduction of this article is prohibited.

Downloaded 08/22/21 to 130.215.63.230. Redistribution subject to SIAM license or copyright; see https://epubs.siam.org/page/terms

to the governing equations can accurately approximate the macroscale behavior. This approach has many limitations, which include being unable to account for the wave-geometry interactions that occur at high frequencies. Most notably, however, is that model accuracy decreases as the bulk and inclusion constituent materials approach the percolation threshold, which is the state of most porous media. The EM heating applications we consider require modeling both of these conditions.

In contrast multiple-scale homogenization attempts to average the governing equations over the microscale to generate an effective equation instead of an effective parameter. It has been widely applied to Maxwell's equations and include studies involving lossless media at low-frequency [30, 23, 36, 34, 60, 54, 22, 57, 52], dissipative media at low-frequency [59, 4, 2, 9], lossless media at high-frequency [34, 14, 22], and finally lossy media at high-frequency [2]. There are also a few studies into the transition region between low- and high-frequency régimes [2, 10]. Most of the homogenization models only consider the closed domain problem which assume an external boundary of a perfect conductor. Of greater interest is the open domain scattering problem, where there is an applied external field. It models applications such as solar thermal heating or beamed energy more accurately. Hence, much of the literature on EM homogenization is incompatible with high-frequency dielectric heating. High-frequency dielectric heating is of interest because it has been shown that new stable steady-state temperatures can be achieved under the application of Bragg resonance with a defect cavity [20, 48, 19]. This is a well known phenomenon in the study of photonic crystals; however, it has not been considered for heating applications until now.

As a result we develop a high-frequency homogenization (HFH) capable of including a temperature dependent dielectric loss. Craster, Kaplunov, and Pichugin [14] developed a HFH for the lossless acoustic problem in two dimensions. It determines approximations to dispersion curves via perturbations away from the periodic and antiperiodic solutions by applying the Floquet–Bloch theory. We extend this work to the curl-curl formulation of Maxwell's equations for a low-loss dielectric in three dimensions.

Section 2 reviews the EM theory utilized in the homogenization. We also discuss three possible asymptotic regimes on the dielectric loss and when they are applicable. Section 3 develops the general homogenization procedure for the low-loss high-frequency materials in three dimensions. A one-dimensional (1D) example is verified against the exact solution found by using the Transfer Matrix Method (TMM) in section 4. In section 5, we consider the impact of the volume fraction of the lossless material in this example at these resonant frequencies for the onset of thermal runaway. Finally, conclusions are discussed in section 6.

2. Problem formulation.

Consider an infinite slab, thickness L, composed of two different dielectric materials, and periodic in each spatial dimension, where $\boldsymbol{\xi}$ is our local coordinate system, as shown in Figure 1. One of the materials has a loss factor which depends on temperature. An electromagnetic wave propagates through the slab in the z-direction. We are interested in the heating of this slab by this applied field for the case when the wavelength of the applied field is comparable to the characteristic spatial microscale period ℓ of the composite pattern.

Maxwell's equations, which govern the electromagnetic behavior of this system, can be restated for the time harmonic solutions $\mathbf{E}(\mathbf{x}) = e^{-i\omega\, t}\,\mathbf{E}(\mathbf{x})$, in the curl-curl

Copyright © by SIAM. Unauthorized reproduction of this article is prohibited.

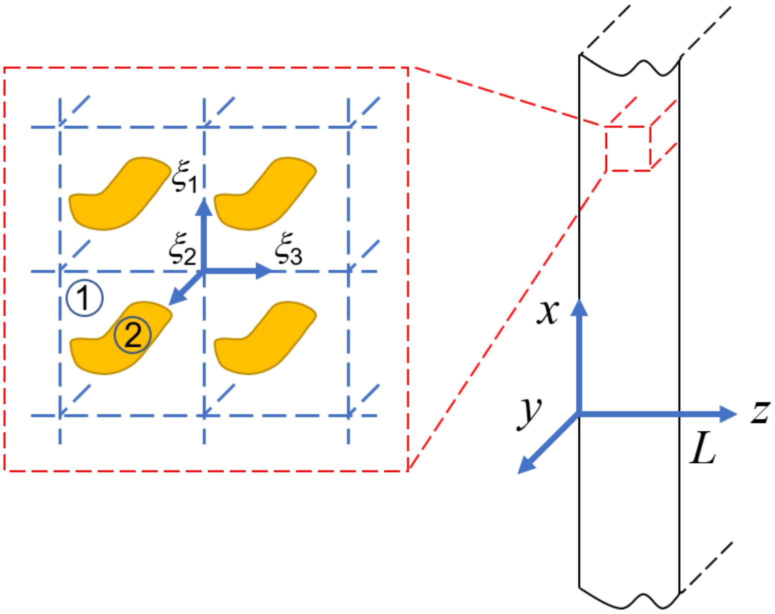

Fig. 1. *Patterned microscale structure along with the macroscale coordinate systems/dimensions.*

formulation

$$\nabla \cdot (\epsilon\, \mathbf{E}) = 0, \tag{1}$$

$$\nabla^2 \mathbf{E} + \gamma^{*2} \epsilon \mathbf{E} - \nabla(\nabla \cdot \mathbf{E}) = 0, \tag{2}$$

where $\mathbf{E}(\mathbf{x})$ is the time-harmonic electric field and $\gamma^* = \omega\sqrt{\epsilon_o\,\mu_o}$ is the free space wavenumber of the applied plane wave.[1] The nondimensional dielectric constant ϵ depends on the local material:

$$\epsilon = \begin{cases} \epsilon_1 & \text{material } 1, \\ \epsilon_2 - i\,\chi_2((T - T_o)/T_o) & \text{material } 2, \end{cases} \tag{3}$$

where ϵ_j is the permittivity of each material $j = 1, 2$, and the loss factor χ_j is zero in material 1 and a function of temperature in the lossy material 2, referenced at the ambient temperature T_o. In the analysis below, we used the index $j = 1, 2$ to denote the domain of material 1, 2, respectively. While the dielectric constants can depend on temperature, the loss factor's temperature dependence is more significant and relevant in this electromagnetic-heating application.

The local temperature of the material is governed by the energy equation

$$\rho_j\, c_{p,j} \frac{\partial T}{\partial t} = k_j \nabla^2 T + \frac{\epsilon_o\, \omega\, \chi_j((T - T_o)/T_o)}{2} \left|\mathbf{E}(\mathbf{x})\right|^2 , \tag{4}$$

where ρ_j is the mass density of material j, $c_{p,j}$ is the specific heat, and k_j is the thermal conductivity for $j = 1, 2$. Here, we assume that the time-scale of energy

---

[1] While this system appears to be overdetermined, both equations are required as per Jackson [24, sect. 6.2ff].

Downloaded 08/22/21 to 130.215.63.230. Redistribution subject to SIAM license or copyright; see https://epubs.siam.org/page/terms

Copyright © by SIAM. Unauthorized reproduction of this article is prohibited.

Downloaded 08/22/21 to 130.215.63.230. Redistribution subject to SIAM license or copyright; see https://epubs.siam.org/page/terms

transport is much longer than the temporal period of the applied electromagnetic plane wave.

We assume perfect thermal contact along the boundary Ω between the two materials, and assume there is no free charge throughout the medium:

$$T\big|_1^2 = 0,\ k_j \nabla T \cdot \mathbf{n}\big|_1^2 = 0\ , \quad \mathbf{x} \in \Omega, \tag{5}$$

$$\epsilon\,\mathbf{E}\cdot\mathbf{n}\big|_1^2 = 0,\ \mathbf{E}\times\mathbf{n}\big|_1^2 = 0\ ,\ (\nabla\times\mathbf{E})\cdot\mathbf{n}\big|_1^2 = 0\ ,\ \mathbf{n}\times(\nabla\times\mathbf{E})\big|_1^2 = \mathbf{0}\ , \quad \mathbf{x}\in\Omega\ , \tag{6}$$

where the notation $f\big|_1^2 = f_2 - f_1$ is the jump condition in the quantity f from region $j = 2$ to region $j = 1$, and $\mathbf{n}$ is a unit normal vector along Ω.

To arrive at a nondimensionalization of (4)–(6), we scale $\mathbf{E}$ on E_o, the amplitude of the applied electromagnetic wave in free space, $T = T_o\,(1+\theta)$ is the temperature, with T_o being the ambient temperature surrounding the slab, and θ being the relative change of temperature from ambient. We are interested here in time-harmonic solutions (or solutions that are steady-state on the heat transfer time scale), and we scale lengths on the slab thickness L to arrive at the system

$$\nabla\cdot(\epsilon\,\mathbf{E}) = 0, \tag{7}$$

$$\nabla^2\mathbf{E} + \left(\frac{\gamma}{\eta}\right)^2 \epsilon\,\mathbf{E} - \nabla(\nabla\cdot\mathbf{E}) = 0, \tag{8}$$

$$\frac{k_j}{k_1}\,\nabla^2\theta + P\,\chi_j(\theta)\ |\mathbf{E}|^2 = 0, \tag{9}$$

where $\gamma = \ell\gamma^*$, $P = \ell^2\,\epsilon_o\,\omega\,|E_o|^2/(k_1\,T_o)$ is the power parameter, and $\eta = \ell/L \ll 1$ is the aspect ratio of the geometric periodicity of the composite pattern and the slab thickness. Boundary conditions (5), (6) can be written as

$$\theta_j\Big|_1^2 = 0\ ,\ \frac{k_j}{k_1}\nabla\theta_j\,\cdot\mathbf{n}\Big|_1^2 = 0\ ,\ \ \mathbf{x}\in\partial\Omega, \tag{10}$$

$$\begin{aligned} &\epsilon\,\mathbf{E}_j\cdot\mathbf{n}\big|_1^2 = 0,\ \mathbf{E}_j\times\mathbf{n}\big|_1^2 = \mathbf{0}\ ,\\ &\qquad(\nabla\times\mathbf{E}_j)\cdot\mathbf{n}\big|_1^2 = 0\ ,\ \ \mathbf{n}\times(\nabla\times\mathbf{E}_j)\big|_1^2 = \mathbf{0}\ ,\ \ \mathbf{x}\in\partial\Omega\ . \end{aligned} \tag{11}$$

Note that the volume contained in Ω is bounded above by η^3, or the volume of the unit periodic cell structure.

3. Model derivation.

Since we are interested in wavelengths that are comparable to the spatial period of the microstructure, we consider a scale separation, where $\boldsymbol{\xi} = \mathbf{x}/\eta$ are the variables on the microscale when $\eta \ll 1$. We further restrict ourselves to steady-state solutions, and assume that $\mathbf{E} = \mathbf{E}(\boldsymbol{\xi},\mathbf{x}), \theta = \theta(\boldsymbol{\xi},\mathbf{x})$ are now functions of both $\boldsymbol{\xi}$ and $\mathbf{x}$, with the θ periodic on the microscale, but $\mathbf{E}$ being either periodic or antiperiodic over each component $\xi_\ell,\ \ell = 1,2,3$, resulting in eight different potential solution states. In addition, we assume that $\epsilon_j = O(1),\ \chi_2(0) = O(\eta^2)$, or that the amount of power absorbed by the lossy material is $O(\eta^2)$.

We define the following asymptotic expansions for Maxwell's equations, analogous to [14]

$$\mathbf{E} = \mathbf{E}^{(0)} + \eta\mathbf{E}^{(1)} + \eta^2\mathbf{E}^{(2)} + \cdots\ , \quad \gamma^2 = \gamma_o^2 + \eta\gamma_1^2 + \eta^2\gamma_2^2 + \cdots\ ,$$

along with a similar expansion for the temperature θ,

$$\theta = \theta^{(0)} + \eta\theta^{(1)} + \eta^2\theta^{(2)} + \cdots\ ,$$

Copyright © by SIAM. Unauthorized reproduction of this article is prohibited.

Downloaded 08/22/21 to 130.215.63.230. Redistribution subject to SIAM license or copyright; see https://epubs.siam.org/page/terms

where each of the $\mathbf{E}^{(m)}, \theta^{(m)}$ are functions of $\boldsymbol{\xi}, \mathbf{x}$, and t. Next, we apply multiple scales in space so that the ∇ operator in (7)–(9) becomes

$$\nabla = \frac{1}{\eta}\,\nabla_\xi + \nabla_x\ ,$$

where ∇_ξ is the gradient operator only on the microscale variables $\boldsymbol{\xi}$, and ∇_x is the gradient operator only on the macroscale variables $\mathbf{x}$. The Laplacian operator with this assumption is given by

$$\nabla^2 = \frac{1}{\eta^2}\,\nabla_\xi^2 + \frac{1}{\eta}\left(\mathrm{div}_x\nabla_\xi + \mathrm{div}_\xi\nabla_x\right) + \nabla_x^2\ .$$

For scale separation, we require that $\mathbf{E}, \theta$ remain bounded as $|\boldsymbol{\xi}| \to \infty$. Classically, boundedness requires that these quantities are periodic over the periodic cell $\mathcal{V}$, defined as

$$\mathcal{V} = \{\boldsymbol{\xi}\ \ |\ \ -1 \le \xi_i \le 1\ ,\ i = 1,2,3\}\ .$$

However, in the propagation of electric fields through lossless composite media, it is of interest to look at cases for which $\mathbf{E}$ is periodic over one component $\xi_i \in [-2,2]$, while the other components are periodic on $[-1,1]$ [27]. We say that $\mathbf{E}$ is the *antiperiodic* in the ξ_i-component. In fact, there are eight different sets of periodic boundary conditions for which each component can be periodic or antiperiodic. The implications of these different cases are addressed as we proceed through the asymptotic solution.

The leading-order problem at $O(\eta^{-2})$ is given by

$$\nabla_\xi \cdot (\epsilon_j \mathbf{E}_j^{(0)}) = 0, \tag{12}$$

$$\nabla_\xi^2 \mathbf{E}^{(0)} + \gamma_0^2 \epsilon_j \mathbf{E}_j^{(0)} - \nabla_\xi(\nabla_\xi \cdot \mathbf{E}_j^{(0)}) = \mathbf{0}, \tag{13}$$

$$\nabla_\xi^2 \theta_j^{(0)} = 0, \tag{14}$$

with $\mathbf{E}^{(0)}$ one of the eight states described above on $\mathcal{V}$, and $\theta^{(0)}$ periodic on $\mathcal{V}$. Further, the following boundary conditions on $\Omega \subset \mathcal{V}$ are required:

$$\theta_j^{(0)}\Big|_1^2 = 0\ ,\ \ \frac{k_j}{k_1}\,\nabla_\xi \theta_j^{(0)}\ \cdot \mathbf{n}\Big|_1^2 = 0\ ,\quad \boldsymbol{\xi} \in \partial\Omega, \tag{15}$$

$$\begin{gathered}\epsilon_j\,\mathbf{E}_j^{(0)} \cdot \mathbf{n}\Big|_1^2 = 0\ ,\ \ \mathbf{E}_j^{(0)} \times \mathbf{n}\Big|_1^2 = 0\ ,\\ \left(\nabla_\xi \times \mathbf{E}_j^{(0)}\right) \cdot \mathbf{n}\Big|_1^2 = 0\ ,\ \ \mathbf{n} \times \left(\nabla_\xi \times \mathbf{E}_j^{(0)}\right)\Big|_1^2 = \mathbf{0}\ ,\quad \boldsymbol{\xi} \in \partial\Omega\ ,\end{gathered} \tag{16}$$

where ϵ_j is the real part of the permittivity ϵ in material j.

Note that at leading order the electric field and the temperature decouple, and each quantity can be addressed individually. Coupling between these two quantities do not appear until $O(1)$, and so in the following we focus on the leading-order solution and the $O(\eta)$ correction for the electric field. For the temperature, the result is classical (e.g., see [45]), and we discuss the energy equation after determining the effective equation for the electric field. Note that the leading-order temperature is given by $\theta_j^{(0)}(\boldsymbol{\xi}, \mathbf{x}) = \theta^{(0)}(\mathbf{x})$.

For the electric field we are interested in nontrivial solutions, and we define the pair $(\mathbf{U}^{(0)}, \gamma_0)$ as the eigenfunction and corresponding eigenvalue to the solution of (12), (13) subject to (16) and either periodic or antiperiodic boundary conditions in

Copyright © by SIAM. Unauthorized reproduction of this article is prohibited.

Downloaded 08/22/21 to 130.215.63.230. Redistribution subject to SIAM license or copyright; see https://epubs.siam.org/page/terms

each direction along $\partial\mathcal{V}$. This set contains eight different base-state solutions, each with its corresponding eigenvalue γ_0. These form a subset of the Bloch modes which are found in the study of photonic crystals [27]. Practically, this solution would need to be computed numerically for a particular set of materials and Ω, but we formally proceed in our analysis assuming γ_0 has a geometric multiplicity of one.

The system (12)–(16) is linear, and the leading-order solution for $\mathbf{E}^{(0)}$ in general is a 3×3 tensor that depends on $\mathbf{x}$ times the base state in ξ

$$\mathbf{E}^{(0)} = \mathbf{F}(\mathbf{x})\, \mathbf{U}^{(0)}(\boldsymbol{\xi}, \gamma_o) \ , \tag{17}$$

where the amplitude of the field depends on the macroscale, along with its polarization. For simplicity in its derivation, we consider polarizations that do not depend on the macroscale at leading order, given by the net polarization of $\mathbf{U}^{(0)}$ over $\mathcal{V}$, and use the solution form

$$\mathbf{E}^{(0)} = f^{(0)}(\mathbf{x})\mathbf{U}^{(0)}(\boldsymbol{\xi}, \gamma_0). \tag{18}$$

The set of solutions $\mathbf{U}^{(0)}(\boldsymbol{\xi}, \gamma_o)$, in general, are a collection of discrete states called the Bloch states, with the eigenvalues denoted as the Bloch spectra [27]. These states for lossless media are, in general, periodic along a lattice vector $\mathbf{a}$, which gives the additional constraint in the lossless case for $f^{(0)}(\mathbf{x}) = f^{(0)}(\mathbf{x} + \eta\, R\, \mathbf{a})$, where R is some distance, in terms of $\boldsymbol{\xi}$ between the different cells. These results rely on symmetry arguments of the media and Maxwell's equations at a fixed frequency, and any dielectric loss in the components of the media break these symmetry arguments. Our asymptotic approach here allows us to explore the impact of these thermal losses on this family of solutions.

At $O(\eta^{-1})$, we have the system

$$\nabla_\xi \cdot (\epsilon_j \mathbf{E}_j^{(1)}) = -\nabla_x \cdot (\epsilon_j\, \mathbf{E}_j^{(0)}), \tag{19}$$

$$\begin{aligned} \nabla_\xi^2 \mathbf{E}_j^{(1)} + \gamma_0^2 \epsilon_j \mathbf{E}_j^{(1)} - \nabla_\xi(\nabla_\xi \cdot \mathbf{E}_j^{(1)}) &= \nabla_\xi \left(\nabla_x \cdot \mathbf{E}_j^{(0)}\right) + \nabla_x \left(\nabla_\xi \cdot \mathbf{E}_j^{(0)}\right) \\ &\quad - \nabla_x \cdot (\nabla_\xi \mathbf{E}_j^{(0)}) - \nabla_\xi \cdot (\nabla_x \mathbf{E}_j^{(0)}) - \gamma_1^2\, \epsilon_j \mathbf{E}_j^{(0)}, \end{aligned} \tag{20}$$

subject to the jump conditions along $\partial\Omega$,

$$\begin{aligned} &\epsilon_j\, \mathbf{E}_j^{(1)} \cdot \mathbf{n} \Big|_1^2 = 0, \mathbf{E}_j^{(1)} \times \mathbf{n} \Big|_1^2 = \mathbf{0} \ , \\ &\left(\nabla_\xi \times \mathbf{E}_j^{(1)}\right) \cdot \mathbf{n} \Big|_1^2 = -\left(\nabla_x \times \mathbf{E}_j^{(0)}\right) \cdot \mathbf{n} \Big|_1^2 \ , \\ &\mathbf{n} \times \left(\nabla_\xi \times \mathbf{E}_j^{(1)}\right) \Big|_1^2 = -\,\mathbf{n} \times \left(\nabla_x \times \mathbf{E}_j^{(0)}\right) \Big|_1^2 \ , \ \boldsymbol{\xi} \in \partial\Omega \ , \end{aligned} \tag{21}$$

along with the appropriate periodic boundary conditions on $\partial\mathcal{V}$, corresponding to which of the eight states $\mathbf{E}^{(0)}$ corresponds.

Before constructing the solution $\mathbf{E}^{(1)}$, we require that the right-hand side of (20) needs to be orthogonal to $\mathbf{U}^{(0)}$ based on the inner product

$$\langle \mathbf{U}, \mathbf{W} \rangle = \int_{\mathcal{V}} \mathbf{U}^H \mathbf{W}\, dV \ , \tag{22}$$

where $\mathbf{U}^H$ is the Hermitian transpose of $\mathbf{U}$. Compatability requires that no resonant modes of the linear operator are driven by the inhomogeneity in the system. From Appendix A, we find $\gamma_1^2 = 0$ in (20).

Copyright © by SIAM. Unauthorized reproduction of this article is prohibited.

Downloaded 08/22/21 to 130.215.63.230. Redistribution subject to SIAM license or copyright; see https://epubs.siam.org/page/terms

Formally, (19)–(21) can be solved in terms of f and $\mathbf{U}^{(0)}$, and from the details shown in Appendix A we find

$$\mathbf{E}^{(1)} = f^{(1)}\mathbf{U}^{(0)} + \left[\underline{\underline{V}} - \mathbf{U}^{(0)}\boldsymbol{\xi}^T\right] \nabla_x f^{(0)} , \tag{23}$$

where $\mathbf{V}_j(\boldsymbol{\xi})$ is the jth column vector of tensor $\underline{\underline{V}}(\boldsymbol{\xi})$ and represents solutions which are neither periodic or antiperiodic solutions of the leading-order electromagnetic system in the ξ_i-direction. Requiring periodicity of $\mathbf{E}^{(1)}$ yields the following conditions on $\underline{\underline{V}}$: the tensor elements v_{21}, v_{31}, v_{22}, v_{32}, v_{23}, v_{33} are periodic in ξ_1; tensor elements v_{11}, v_{31}, v_{12}, v_{32}, v_{13}, v_{33} are periodic in ξ_2; and tensor elements v_{11}, v_{21}, v_{12}, v_{22}, v_{13}, v_{23} are periodic in ξ_3. It also requires the application of jump conditions are

$$v_{ji}\big|_{\xi_i=1} - v_{ji}\big|_{\xi_i=-1} = 2U_j^{(0)}\Big|_{\xi_i=1} \tag{24}$$

for $i, j = 1, 2, 3$. We also require that $\frac{\partial \mathbf{E}^{(1)}}{\partial \xi_k}$ is periodic in ξ_k. This implies that $\frac{\partial v_{ji}}{\partial \xi_k}$ is periodic in ξ_k for $k \neq i$, and jump conditions

$$\left.\frac{\partial v_{ji}}{\partial \xi_i}\right|_{\xi_i=1} - \left.\frac{\partial v_{ji}}{\partial \xi_i}\right|_{\xi_i=-1} = 2 \left.\frac{\partial U_j^{(0)}}{\partial \xi_i}\right|_{\xi_i=1} . \tag{25}$$

At $O(1)$, we focus on the closure condition on $f^{(0)}$. The curl-curl relation (8) at this order is given by

$$\begin{aligned}\nabla_\xi^2\mathbf{E}^{(2)} + \gamma_0^2\, \epsilon_j\, \mathbf{E}^{(2)} - \nabla_\xi \left(\nabla_\xi \cdot \mathbf{E}^{(2)}\right) = {}& \nabla_\xi(\nabla_x \cdot \mathbf{E}^{(1)}) + \nabla_x(\nabla_\xi \cdot \mathbf{E}^{(1)}) + \nabla_x(\nabla_x \cdot \mathbf{E}^{(0)}) \\ & - \nabla_x \cdot (\nabla_\xi \mathbf{E}^{(1)}) - \nabla_\xi \cdot (\nabla_x \mathbf{E}^{(1)}) - \nabla_x^2\mathbf{E}^{(0)} \\ & + i\gamma_0^2\, \chi_j\, \mathbf{E}^{(0)}. \end{aligned} \tag{26}$$

The compatibility condition defines the differential equation for $f^{(0)}(\mathbf{x})$ as

$$\nabla_x \cdot \left[\underline{\underline{T}}\nabla_x f^{(0)}\right] + \left[\gamma_2^2 + iD\right] f^{(0)} = 0, \tag{27}$$

where scalar D is given by

$$D = \frac{-\int_{\partial\mathcal{V}}(\epsilon_j)^{-1}\left[(\nabla_\xi\chi_j(\theta^{(0)}(\mathbf{x}))) \cdot \mathbf{U}^{(0)}\right]\left(\mathbf{U}^{(0)} \cdot \mathbf{n}\right)\, dS + \gamma_0^2 \int_{\mathcal{V}} \chi_j(\theta^{(0)}(\mathbf{x}))\, |\mathbf{U}^{(0)}|^2\, dV}{\int_{\mathcal{V}} \epsilon_j |\mathbf{U}^{(0)}|^2\, dV}, \tag{28}$$

and the elements of tensor $\underline{\underline{T}}$ are $T_{ij} = \frac{t_{ij}}{\int_{\mathcal{V}} \epsilon_j |\mathbf{U}^{(0)}|^2\, dV}$, where

$$t_{jk} = \int_{\mathcal{V}} \left[\frac{\partial v_{ik}}{\partial \xi_j} U_i^{(0)} + \frac{\partial v_{ij}}{\partial \xi_k} U_i^{(0)}\right] dV, \tag{29}$$

$$t_{kk} = 2\int_{\mathcal{V}} \frac{\partial v_{ik}}{\partial \xi_k} U_i^{(0)}\, dV - 2\iint \left(U_i^{(0)}\right)^2\Big|_{\xi_k=1} d\xi_p d\xi_q, \tag{30}$$

where $p, q \neq k$. Solving (27) for the macroscale dependence $f^{(0)}(\mathbf{x})$ closes the leading-order problem, and providing a net representation for the electric field $\mathbf{E}^{(0)}$.

To close the problem, we need to determine the effective equation for the temperature $\theta^{(0)}(\mathbf{x})$. Following section 2.2 in Mei and Vernescu [45], the leading- and

Copyright © by SIAM. Unauthorized reproduction of this article is prohibited.

Downloaded 08/22/21 to 130.215.63.230. Redistribution subject to SIAM license or copyright; see https://epubs.siam.org/page/terms

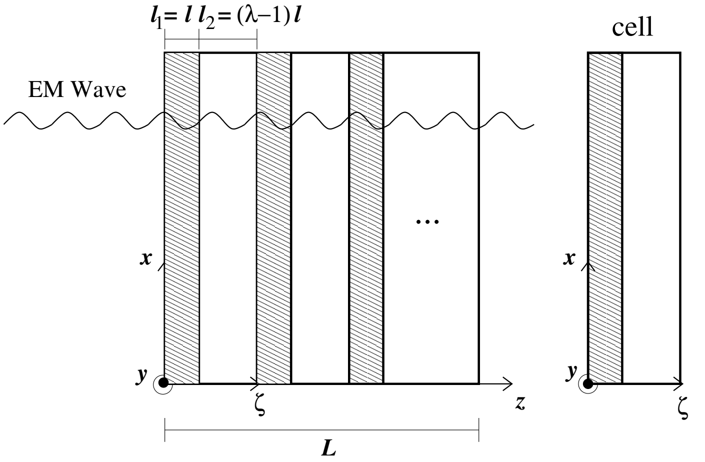

FIG. 2. *Left: Schematic of* 1*D example as a periodic array of slabs, with plane waves applied from* $z \to -\infty$ *and propagating through the medium. Right: Cell problem for microscale solution.*

first-order correction follows their derivation of the homogeneous problem. Since our inhomogeneity enters at $O(1)$, we arrive at the effective equation

$$\nabla_x \left\{ \mathcal{K} \nabla_x \, \theta^{(0)} \right\} + \frac{1}{8} \, P \int_{\mathcal{V}} \chi(\theta^{(0)}(\mathbf{x})) \, |\mathbf{E}^{(0)}(\boldsymbol{\xi}, \mathbf{x})|^2 \, dV = 0 \; . \tag{31}$$

The final set of coupled elliptic equations to solve are (28), (32), for the electric field amplitude $f^{(0)}$ and the temperature $\theta^{(0)}$ over $\mathbf{x}$, subject to appropriate boundary conditions on the composite.

4. 1D example.

We consider the 1D example of an alternate array of periodic laminates shown by Figure 2. An electromagnetic wave, polarized in the y-direction, propagates in the z-direction, with the lossy layer (gray in Figure 2 of unit length). Here, $\zeta = \xi_3$, no dependence of the electric field on (ξ_1, ξ_2), with $-(\lambda - 1) \leq \zeta \leq 1$, so the spatial period is given by λ. With these assumptions, the electric field is guaranteed to be solenoidal. Applying the techniques from section 3 to this problem, the leading-order solution is given by

$$E^{(0)}(z, \zeta) = f^{(0)}(z) \, \frac{U^{(0)}(\zeta, p)}{||U^{(0)}(\zeta, p)||} \; , \tag{32}$$

where the form of the cell solution is given by

$$U^{(0)}(\zeta, p) = \begin{cases} \sqrt{\epsilon_2} \sin(\gamma_0 \sqrt{\epsilon_1} \zeta) + p \cos(\gamma_0 \sqrt{\epsilon_1} \zeta), & -(\lambda - 1) \leq \zeta \leq, 0, \\ \sqrt{\epsilon_1} \sin(\gamma_0 \sqrt{\epsilon_2} \zeta) + p \cos(\gamma_0 \sqrt{\epsilon_2} \zeta), & 0 \leq \zeta \leq 1, \end{cases} \tag{33}$$

with

$$||U^{(0)}(\zeta, p)||^2 = \int_{-(\lambda-1)}^{1} \left[U^{(0)}(\zeta, p) \right]^2 \, d\zeta \, .$$

For the periodic (antiperiodic) leading-order cell solution, p reduces to

$$p_o = \frac{\sqrt{\epsilon_2} \sin(\gamma_0 \sqrt{\epsilon_1} (\lambda - 1)) \pm \sqrt{\epsilon_1} \sin(\gamma_0 \sqrt{\epsilon_2})}{\cos(\gamma_0 \sqrt{\epsilon_1} (\lambda - 1)) \mp \cos(\gamma_0 \sqrt{\epsilon_2})} \; , \tag{34}$$

Copyright © by SIAM. Unauthorized reproduction of this article is prohibited.

Downloaded 08/22/21 to 130.215.63.230. Redistribution subject to SIAM license or copyright; see https://epubs.siam.org/page/terms

where the plus sign of ± denotes the periodic solution while the negative sign denotes the antiperiodic solution. For this case, the leading-order frequency γ_o solves the dispersion relation

$$\begin{aligned} &2\sqrt{\epsilon_1\,\epsilon_2}\left[\cos\left[\gamma_o\sqrt{\epsilon_1}\,(\lambda-1)\right]\,\cos\left(\gamma_o\sqrt{\epsilon_2}\right)\mp 1\right] \\ &\quad=(\epsilon_1+\epsilon_2)\,\sin\left[\gamma_o\sqrt{\epsilon_1}\,(\lambda-1)\right]\,\sin\left(\gamma_o\sqrt{\epsilon_2}\right)\,. \end{aligned} \tag{35}$$

Following Craster, Kaplunov, and Pichugin [14], the macroscale dependence can be determined by applying the Floquet–Bloch theory on the macroscale,

$$E^{(0)}(z\pm\lambda\eta,\zeta)=e^{i(k+i\kappa)\lambda\eta}E^{(0)}(z,\zeta), \tag{36}$$

which implies that

$$p=\frac{\sqrt{\epsilon_2}\sin(\gamma_0\sqrt{\epsilon_1}(\lambda-1))+e^{\lambda\eta\kappa}\sqrt{\epsilon_1}\sin(\gamma_0\sqrt{\epsilon_2})}{\cos(\gamma_0\sqrt{\epsilon_1}(\lambda-1))-e^{\lambda\eta\kappa}\cos(\gamma_0\sqrt{\epsilon_2})} \tag{37}$$

if we ignore losses in the lossy medium. When losses are present, we let

$$f^{(0)}(z)=e^{\pm(-\kappa+ik)z} \tag{38}$$

for the periodic case and

$$f^{(0)}(z)=e^{\pm(-\kappa+i(k-\frac{\pi}{\lambda\eta}))z} \tag{39}$$

for the antiperiodic case. The equations relating γ_2 to k and κ are found by substituting $f^{(0)}$ into the 1D version of (27) yielding

$$k^2-\kappa^2=\frac{-\gamma_2^2\int_{-(\lambda-1)}^{1}\epsilon_j\,(U^{(0)}(\zeta,p_o))^2\,d\zeta}{\left[\lambda(U^{(0)}(1,p_o))^2-2A\int_{-(\lambda-1)}^{1}V_\zeta(\zeta,p_o)U^{(0)}(\zeta,p_o)\,d\zeta\right]}=\gamma_2^2\epsilon_{eff}, \tag{40}$$

$$-2k\kappa=\frac{-\gamma_0^2\int_{-(\lambda-1)}^{1}\chi_j(U^{(0)}(\zeta,p_o))^2\,d\zeta}{\left[\lambda(U^{(0)}(1,p_o))^2-2A\int_{-(\lambda-1)}^{1}V_\zeta(\zeta,p_o)U^{(0)}(\zeta,p_o)\,d\zeta\right]}=\gamma_0^2\chi_{eff} \tag{41}$$

for the periodic case and

$$\left(k-\frac{\pi}{\lambda\eta}\right)^2-\kappa^2=\frac{-\gamma_2^2\int_{-(\lambda-1)}^{1}\epsilon_j(U^{(0)}(\zeta,p_o))^2\,d\zeta}{\left[\lambda(U^{(0)}(1,p_o))^2-2A\int_{-(\lambda-1)}^{1}V_\zeta(\zeta,p_o)U^{(0)}(\zeta,p_o)\,d\zeta\right]}=\gamma_2^2\epsilon_{eff}, \tag{42}$$

$$-2\left(k-\frac{\pi}{\lambda\eta}\right)\kappa=\frac{-\gamma_0^2\int_{-(\lambda-1)}^{1}\chi_j(U^{(0)}(\zeta,p_o)^2\,d\zeta}{\left[\lambda(U^{(0)}(1,p_o))^2-2A\int_{-(\lambda-1)}^{1}V_\zeta(\zeta,p_o)U^{(0)}(\zeta,p_o)\,d\zeta\right]}=\gamma_0^2\chi_{eff} \tag{43}$$

for the antiperiodic case.

For clarity, defining the quantities (40), (41) as effective dielectric constant and effective dielectric loss they closely resemble similar equations for a *homogeneous* medium

$$k^2-\kappa^2=\epsilon, \tag{44}$$

$$-2k\kappa=\chi\ , \tag{45}$$

Copyright © by SIAM. Unauthorized reproduction of this article is prohibited.

Downloaded 08/22/21 to 130.215.63.230. Redistribution subject to SIAM license or copyright; see https://epubs.siam.org/page/terms

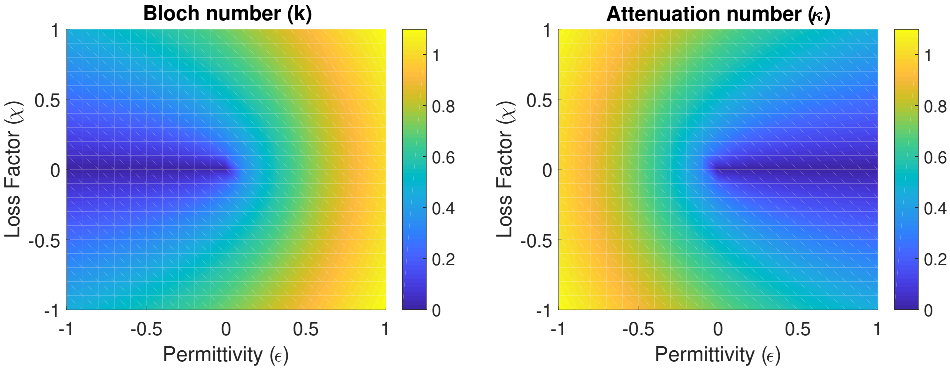

(a) (b)

Fig. 3. *Complex wavenumber as a function of permittivity* ϵ *and loss factor* χ. (a) *Imaginary part of the wavenumber, the Block number* k *from* (46), *and* (b) *real part of the wavenumber, or the attenuation number* κ *from* (47).

where

$$\lambda^2\eta^2\gamma_2^2\epsilon_{eff} \to \epsilon \ , \quad \lambda^2\eta^2\gamma_o^2\chi_{eff} \to \chi \ , \quad \lambda\eta k \to k \ , \quad \lambda\eta\kappa \to \kappa \ .$$

Note that a similar transformation can be done for the effective dielectric loss in the antiperiodic case (42), (43). The system (44), (45) for the homogeneous medium can be solved for k and κ as

$$k = \pm\sqrt{\frac{\sqrt{\epsilon^2+\chi^2}+\epsilon}{2}}, \tag{46}$$

$$\kappa = \pm\sqrt{\frac{\sqrt{\epsilon^2+\chi^2}-\epsilon}{2}}. \tag{47}$$

The plots of (46) and (47) are shown in Figures 3a and 3b and provide insight into the behavior of the homogenized solution.

The relationship between k, κ, ϵ, and χ can be classified into four different cases, as observed in Figure 3. Case 1: all points along $\epsilon > 0$, $\chi = 0$ yield nonattenuated traveling waves $k \neq 0$, $\kappa = 0$. Case 2: all points along $\epsilon < 0$, $\chi = 0$ yield strongly attenuated nonpropagating waves $k = 0$, $\kappa \neq 0$. Case 3: points in the right half plane, where $\epsilon > 0$, $\chi \neq 0$ yield traveling waves with weak attenuation, k large, κ small. Case 4: points in the left half plane $\epsilon < 0$, $\chi \neq 0$ yield traveling waves with strong attenuation.

The plots in Figure 3 convey some important consequences. There are only two ways for waves to be attenuated: by loss to the material $\chi \neq 0$ and reflection of waves $\epsilon < 0$. Case 1 refers to the waves produced from a lossless material outside a band gap. Band gaps which are particular frequencies at which waves cannot propagate through the medium only exist in case 2 for no dielectric losses [27]. The moment dielectric losses are introduced k can no longer be zero, allowing for propagation of waves. Despite this, the negative permittivity still yields large attenuation from reflections, called evanescent waves. This is a characteristic feature of the 1D photonic crystal as they are also known as dielectric mirrors or Bragg mirrors since they are nonmetallic materials that produce large reflections. No purely homogeneous material is known to have a negative permittivity. The concept of negative permittivity

Copyright © by SIAM. Unauthorized reproduction of this article is prohibited.

Downloaded 08/22/21 to 130.215.63.230. Redistribution subject to SIAM license or copyright; see https://epubs.siam.org/page/terms

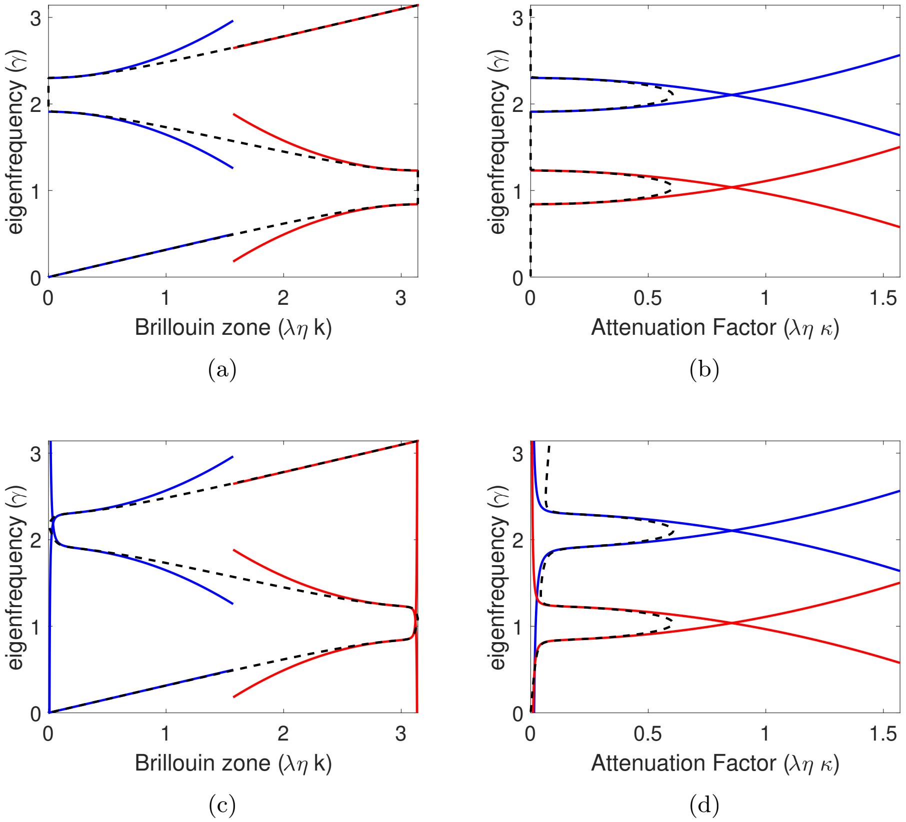

(a) (b)

(c) (d)

FIG. 4. *Comparison of dispersion curves for lossless and lossy effective materials in the* 1*D example with* $\lambda = 2$*,* $\eta = 0.01$*,* $\epsilon_1 = 1$*,* $\epsilon_2 = 4$*. Dashed curves correspond to the computed dispersion curve, while solid curves denote the asymptotic approximation.* (a) *Bloch number* k *as a function of* γ *for a lossless materials;* (b) *attenuation number* κ *as a function of* γ *for lossless materials;* (c) *Bloch number* k *as a function of* γ *for a lossy material,* $\chi_2 = 0.1$*; and* (d) *attenuation number* κ *for a lossy medium with* $\chi_2 = 0.1$*. (Figure in color online.)*

was first hypothesized by Veselago in the 1960s [58]. Since then many such materials possessing an effective negative permittivity have be made and are known as metamaterials, negative index materials, or left-handed materials [41].

Returning to the 1D example, the variable groups $\lambda\eta k$ and $\lambda\eta\kappa$ represent the Brillouin zone and attenuation variables. The eigenfrequency is plotted against these variables to produce the dispersion curves shown in Figure 4 that relate γ to k and κ. The exact dispersion relation between γ and the Bloch and attenuation numbers are shown in dashed curves in this figure. The periodic base state corresponds to $\lambda\eta k = 0$, while the antiperiodic base state corresponds to $\lambda\eta k = \pi$. The solid (blue) curves are asymptotic approximations to the dispersion curve perturbed away from the periodic base state, while the solid (red) curves are asymptotic approximations to the dispersion curve perturbed away from the antiperiodic base state. Figures 4a and 4b plot the Brillouin zone and attenuation curves for a lossless medium. Figure 4a reproduces the findings of [14]. The dispersion curves for the lossless case show the existence of band gaps, i.e., frequency intervals, where no wave propagation can occur. The curves show large attenuation within the band gap regions which correspond to

Copyright © by SIAM. Unauthorized reproduction of this article is prohibited.

Downloaded 08/22/21 to 130.215.63.230. Redistribution subject to SIAM license or copyright; see https://epubs.siam.org/page/terms

large reflections. As mentioned previously it has been shown that band gaps possess a negative effective permittivity [44, 16, 26]. Corresponding to case 2 of Figure 3a, we expect $k = 0$ and κ to be large.

Once dielectric loss is nonzero, as shown by Figures 4c and 4d, the band gaps no longer exist. Waves which are capable of propagating through the medium though still possess a large attenuation, which corresponds to case 4, the homogeneous medium classification (e.g., see Figure 3a). Finally, as in Case 3 for the homogeneous medium shown in Figure 3a, outside a band gap k is large while κ is small. These curves compare well to the dispersion curves produced by the HFH to those of the associated 1D laminate acoustic problem [28]. Band gaps which are present for lossless media no longer exist once material losses are present. Small attenuation develops outside the band gap regions when losses are present.

It has been shown that the effective permittivity within the band gap of a photonic crystal is negative [44, 16, 26], which explains the large attenuation we see in Figure 4b. Once dielectric losses are introduced, there no longer exist any band gaps as shown by Figure 4c. Despite this, the frequencies that were associated with the band gaps still produce an effectively negative permittivity yielding large attenuation via reflections, as shown by Figure 4d. The same figure also shows that off these band gap frequencies (where there previously was no attenuation) now exhibit small amounts of attenuation due to the dielectric loss. The nonperturbed solution for correction $\gamma_2 = 0$ occurs when $k^2 - \kappa^2 = 0$ away from the periodic or antiperiodic cases. $k^2 - \kappa^2 > 0$ correspond to positive permittivity and posses attenuation solely from dielectric loss, and, conversely, $k^2 - \kappa^2 < 0$ corresponds to a negative permittivity residing within the band gap frequencies and possesses attenuation from dielectric losses as well as reflections. Furthermore, even within the band gap frequencies, the Bloch parameters corresponding to purely periodic (antiperiodic) solutions are no longer attainable in the presence of a lossy material.

The same properties hold in the homogenized solution. The perturbations of the dispersion curves away from the two base states are then given by

$$\gamma \approx \gamma_0 + \frac{(\lambda\eta k)^2}{2\lambda^2\gamma_0\epsilon_{eff}} - \frac{\lambda^2\gamma_0^3(\eta^2\chi_{eff})^2}{8\gamma_0\epsilon_{eff}(\lambda\eta k)^2} \tag{48}$$

for the periodic case and

$$\gamma \approx \gamma_0 + \frac{(\lambda\eta k - \pi)^2}{2\lambda^2\gamma_0\epsilon_{eff}} - \frac{\lambda^2\gamma_0^3(\eta^2\chi_{eff})^2}{8\epsilon_{eff}(\lambda\eta k - \pi)^2} \tag{49}$$

for the antiperiodic case. The perturbation curves in terms of the attenuation factor are

$$\gamma \approx \gamma_0 - \frac{(\lambda\eta\kappa)^2}{2\lambda^2\gamma_0\epsilon_{eff}} + \frac{\lambda^2\gamma_0^3(\eta^2\chi_{eff})^2}{8\epsilon_{eff}(\lambda\eta\kappa)^2}. \tag{50}$$

The parameter group $\eta^2\chi_{eff}$ represents the unscaled or natural effective dielectric constant associated with a dielectric medium of this geometry. The Bloch number expansions (48) and (49) and the attenuation expansion (50) reduce to those found by [14] for the case of a lossless medium when $\chi = 0$. While the attenuation of waves was not explicitly discussed in [14], it is trivial to derive the expression. The perturbation approximations break down when k or κ are $O(\eta)$ making the third term in (48)–(50) $O(1)$. A similar break down of the approximation occurs when k or κ are

Copyright © by SIAM. Unauthorized reproduction of this article is prohibited.

Downloaded 08/22/21 to 130.215.63.230. Redistribution subject to SIAM license or copyright; see https://epubs.siam.org/page/terms

$O(\eta^{-1})$ making the second term in (48)–(50) $O(1)$. The asymptotic approximations derived are only valid for γ_0 that are simple roots of the characteristic equation. The degenerate case when γ_0 has multiplicity two yields no attenuation to leading order and yields a dispersion approximation as found by [14].

Now that we have an understanding of the dispersion relations for a particular monochromatic wave with frequency corresponding to wavenumber γ, we can determine the k and κ that govern the macroscopic behavior and plot the solutions. To test this approach, we consider a quantitative example where $\epsilon_1 = 1$ and $\epsilon_2 = 4$, $\chi_2 \neq 0$. From the dispersion relation (35), the frequency of an incoming wave which undergoes resonance is $\gamma \approx 1.91063323$. In terms of applications for beamed energy harnessing, for a characteristic microscale length of 1 mm, this dimensionless frequency corresponds to approximately 91.2 GHz.

With these materials and operating conditions, we consider a composite slab of N-cells, each cell of length $\lambda > 1$, where a plane electromagnetic wave applied at $\zeta = 0$ and the transmitted wave propagates away from the slab at $\zeta = \lambda N$. Our HFH approach above provides an asymptotic solution this this problem provided that $\eta N = O(1)$. However, this situation is amenable to an exact solution using the Transfer Matrix Method (TMM) [41].

Given $0 < \zeta < \lambda N$, we note for plane wave propagation normal to the slabs, a polarization oriented parallel to any slab interface results in Gauss's law begin automatically satisfied, and hence Helmholtz's equations need to be solved in each material

$$\frac{\partial^2 E_{1,j}}{\partial \zeta^2} + \gamma^2 \epsilon_1 E_{1,j} = 0 \ , \quad j\lambda < \zeta < j\lambda + 1 \ , \tag{51}$$

$$\frac{\partial^2 E_{2,j}}{\partial \zeta^2} + \gamma^2 \epsilon_2 E_{2,j} = 0 \ , \quad j\lambda + 1 < \zeta < \lambda(j+1) \ , \tag{52}$$

where $j = 0, 1, \ldots, N-1$ denotes each cell. At each interface within the composite slab, the field amplitudes are continuous, as are the amplitude gradients with respect to ζ,

$$E_{1,j} = E_{2,j}, \quad \frac{\partial E_{1,j}}{\partial \zeta} = \frac{\partial E_{2,j}}{\partial \zeta} \ , \quad \zeta = j\lambda + 1 \ , \tag{53}$$

$$E_{1,j+1} = E_{2,j}, \quad \frac{\partial E_{1,j+1}}{\partial \zeta} = \frac{\partial E_{2,j}}{\partial \zeta} \ , \quad \zeta = \lambda\,(j+1) \ , \tag{54}$$

where $j = 0, 2, \ldots, N-1$. To solve (51)–(54), we can write each solution

$$E_{m,j} = c_{m,j} e^{i\,\gamma\sqrt{\epsilon_m}\zeta} + d_{m,j} e^{-i\,\gamma\sqrt{\epsilon_m}\zeta} \ , \ m = 1, 2 \ , \ j = 0, 1, \ldots, N-1 \ .$$

Applying the boundary conditions (53), (54) gives a matrix relation between $(c_{1,j}, d_{1,j})$ and $(c_{1,j+1}, d_{1,j+1})$,

$$\begin{pmatrix} c_{1,j+1} \\ d_{1,j+1} \end{pmatrix} = \mathbf{M}_j \begin{pmatrix} c_{1,j} \\ d_{1,j} \end{pmatrix} \ .$$

Hence the product $\mathbf{M}_o \mathbf{M}_1, \ldots, \mathbf{M}_{N-1}$ is called the transfer matrix, and each $\mathbf{M}_j$ is known in closed form. With the radiation boundary conditions outside the slab, described below, the exact solution can be determined.

We now compare the solutions generated by the HFH against the exact solutions determined by the TMM. There are three domains to consider: $\zeta < 0$, $0 < \zeta < \lambda N$,

Copyright © by SIAM. Unauthorized reproduction of this article is prohibited.

Downloaded 08/22/21 to 130.215.63.230. Redistribution subject to SIAM license or copyright; see https://epubs.siam.org/page/terms

and $\zeta > \lambda N$. We can write the form of each of these solutions directly,

$$E_1(\zeta) = a_1 e^{i\gamma\zeta} + b_1 e^{-i\gamma\zeta}\ , \qquad -\infty < \zeta \le 0, \tag{55}$$

$$E_2(\zeta) = a_2 e^{i(k+i\kappa)\eta\zeta} U^{(0)}(g(\zeta), p) + b_2 e^{-i(k+i\kappa)\eta\zeta} U^{(0)}(g(\zeta), p)\ , \qquad 0 \le \zeta \le \lambda N, \tag{56}$$

$$E_3(\zeta) = a_3 e^{i\gamma\zeta} + b_3 e^{-i\gamma\zeta}\ , \qquad \lambda N \le \zeta < \infty, \tag{57}$$

where the coefficients a_m, b_m are determined using the following conditions:

$$\lim_{\zeta\to-\infty}\left(\frac{\partial}{\partial\zeta} + i\gamma\right)(E_1 - 1) = 0, \tag{58}$$

$$E_1(0) = E_2(0), \tag{59}$$

$$\frac{\partial E_1}{\partial\zeta}(0) = \frac{\partial E_2}{\partial\zeta}(0), \tag{60}$$

$$E_2(\lambda N) = E_3(\lambda N), \tag{61}$$

$$\frac{\partial E_2}{\partial\zeta}(\lambda N) = \frac{\partial E_3}{\partial\zeta}(\lambda N), \tag{62}$$

$$\lim_{\zeta\to\infty}\left(\frac{\partial}{\partial\zeta} - i\gamma\right)E_3 = 0, \tag{63}$$

where $g(\zeta) = \operatorname{mod}(\zeta, \lambda) - (\lambda - 1)$ since the argument for $U^{(0)}(\zeta, p)$ is restricted to the cell domain $-(\lambda - 1) \le \zeta \le 1$. Note that in our results below, we consider two different values of p below. Solving the system yields coefficients

$$a_2 = \frac{4\,i\,\gamma}{C\,Q}, \tag{64}$$

$$b_2 = -\frac{B}{D} e^{2i(k+i\kappa)\eta\lambda N} a_2, \tag{65}$$

where

$$Q = \left[1 - \frac{A\,B}{C\,D} e^{2i(k+i\kappa)\eta\lambda N}\right], \tag{66}$$

$$A = [i\gamma - i(k+i\kappa)\eta]U^{(0)}(-(\lambda-1), p) + U^{(0)}_{\zeta}(-(\lambda-1), p), \tag{67}$$

$$B = [i\gamma - i(k+i\kappa)\eta]U^{(0)}(1, p) - U^{(0)}_{\zeta}(1, p), \tag{68}$$

$$C = [i\gamma + i(k+i\kappa)\eta]U^{(0)}(-(\lambda-1), p) + U^{(0)}_{\zeta}(-(\lambda-1), p), \tag{69}$$

$$D = [i\gamma + i(k+i\kappa)\eta]U^{(0)}(1, p) - U^{(0)}_{\zeta}(1, p). \tag{70}$$

Figure 5 compares solutions found by the HFH model with $p = p_o$ against the exact solutions of the TMM. The plots show solutions with very good agreement between the two methods even for $O(1)$ dielectric loss where the HFH begins to break down. Figure 5a has no dielectric loss which reduces our model to that of [14] which we validated against an exact solution. A plot of the absolute error as a function of the asymptotic parameter η for several different loss factors is shown in Figure 6a. It shows the error is linear in η which is what we expect from a leading-order asymptotic solution. It also demonstrates that the error increases as the dielectric loss increases since the lossy solutions are perturbed away from the lossless solutions.

One aspect about the HFH solutions is that the amplitude at $\zeta = 0$ is the same for all of the solutions. Examining the equation for the leading-order solution (32),

Copyright © by SIAM. Unauthorized reproduction of this article is prohibited.

Downloaded 08/22/21 to 130.215.63.230. Redistribution subject to SIAM license or copyright; see https://epubs.siam.org/page/terms

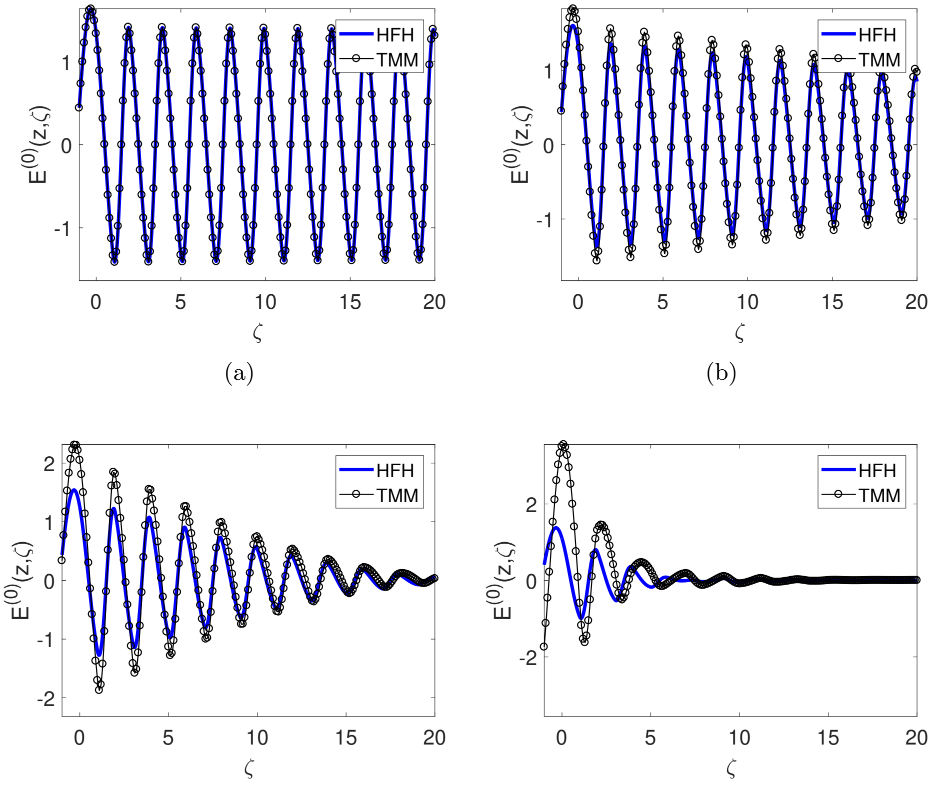

(a) (b)

(c) (d)

FIG. 5. *Comparison of HFH solutions to those of the TMM for a one-sided incident wave of nondimensional wavenumber* $\gamma = 1.91063323$, *which for a characteristic microscale of* $l = 1mm$ *is a frequency* $f = 91.2$ *GHz, impinging a single slab of a heterogeneous laminate of* $2N$ *layers; selected solutions include a two-phase laminate with permittivity* $\epsilon_1 = 1$ *and* $\epsilon_2 = 4$, χ_2 *given below. In all cases,* $p = p_o$. (a) $N = 500$, $\chi_2 = 0$, (b) $N = 500$, $\chi_2 = 0.01$, (c) $N = 50$, $\chi_2 = 0.1$, *and* (d) $N = 50$, $\chi_2 = 1$.

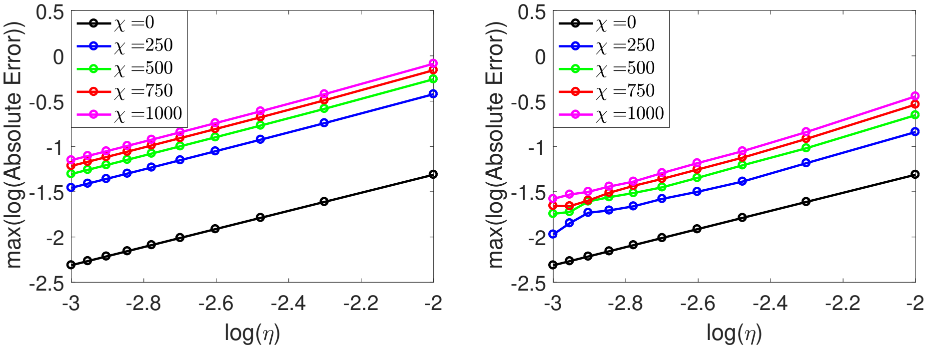

(a) (b)

FIG. 6. *Logarithmic plot of the absolute error between the HFH and the TMM solutions as a function of* η *and several different values for the dielectric loss:* (a) *solutions using* $p = p_o$, (b) *solutions using* $p = p^*$.

Copyright © by SIAM. Unauthorized reproduction of this article is prohibited.

Downloaded 08/22/21 to 130.215.63.230. Redistribution subject to SIAM license or copyright; see https://epubs.siam.org/page/terms

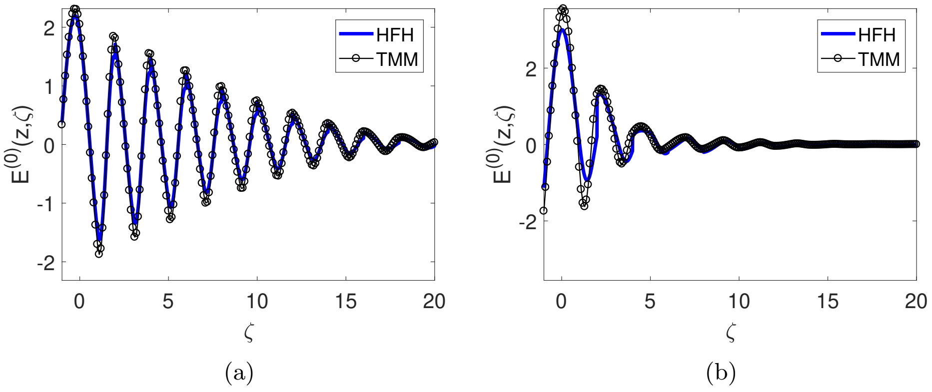

(a) (b)

FIG. 7. *Comparison of HFH solutions to those of the TMM with* $p = p^*$*:* (a) $N = 50$*,* $\chi_2 = 0.1$*,* (b) $N = 50$*,* $\chi_2 = 1$*.*

we note that the only dependence on the dielectric loss appears in the macroscale function $f(z) = e^{(-\kappa+ik)z}$ through the Bloch number k and attenuation number κ. It shows that the amplitude at $\zeta = 0$ remains constant; however, we know that a large dielectric loss will produce large reflections at each of the layer interfaces, increasing the field at $\zeta = 0$, as seen by the TMM in Figures 5c and 5d. Up to this point, we have considered solutions by using (32) with (34). In contrast, now that we have an approximation for k and κ, we substitute these approximations directly into (37), which would then allow the solution to vary its amplitude at $\zeta = 0$. We define this value $p = p^*$. Solutions attained by applying this modification are shown in Figure 7. This substitution yields solutions that fail to satisfy the boundary conditions imposed on the cell problem. Though solutions from this approach fail to satisfy the boundary conditions exactly, since (34) and (37) are asymptotic as $\eta \to 0$, they appear to capture the full solution asymptotically away from the boundary. This alternate method does produce solutions away from the boundary with significantly less error as shown by Figure 6b.

5. Onset of thermal runaway.

If one of the component materials in this composite is a ceramic, then the loss factor can vary significantly over temperature. From the analysis above for periodic media, this suggests that the Bloch parameter and the attenuation parameter both change over temperature, since these parameters both depend on the effective loss factor. Further, the amount of energy absorbed in the effective media depends on this loss factor, and this coupling can result in a phenomenon called *thermal runaway* [64, 63, 62], in which a positive feedback loop is initiated: as temperature increases, the material can better convert the electromagnetic energy to internal energy, which then increases the temperature. The approach used here assumes that the nondimensional temperature deviation from an ambient temperature varies only on the macroscale, and that thermal transport from the medium to the surrounding environment is poor.

We extend the 1D example of section 4 with the inclusion of the energy equation (31). Of particular interest is to determine the power needed for thermal runaway to take place as a function of the cell size λ, and to determine if these values vary based on either a periodic or antiperiodic mode. Since for millimeter-wave applications, the temperature variations in composites scale on lengths much longer than the

Copyright © by SIAM. Unauthorized reproduction of this article is prohibited.

Downloaded 08/22/21 to 130.215.63.230. Redistribution subject to SIAM license or copyright; see https://epubs.siam.org/page/terms

wavelength of the radiation, which is the spatial periodicity of the microscale in this example. Then the leading-order nondimensional energy equation for this example is given by (e.g., [35])

$$\frac{\partial\theta}{\partial t} = A_{har}\frac{\partial^2\theta}{\partial z^2} + \frac{P_l}{\lambda}\,\chi_{eff}(\theta)(t_{22})|f|^2 \ , \tag{71}$$

where θ is the nondimensional temperature deviation from the ambient temperature, and the effective thermal conductivity

$$A_{har} = \frac{\alpha_1\alpha_2\lambda}{\alpha_1 + \alpha_2(\lambda - 1)} \ ,$$

where α_i is the thermal conductivity of material i, and t_{22} is the denominator in the definition (41), (43) of $\epsilon''_{eff}(\theta)$.

Further, we consider a unit width effective material on the macroscale $0 < z < 1$ which is subjected to a plane wave of amplitude 1 at $z = 0$ and transmission conditions at $z = 1$. The envelope $f(z)$ of this electric field is governed by the differential equation

$$f''(z) + \left\{\gamma_2^2\,\epsilon_{eff} - i\,\gamma_0^2\,\chi_{eff}(\theta)\right\}\, f(z) = 0 \ . \tag{72}$$

Hence, the steady-state transmission problem is given by the system

$$f''(z) + \left\{\gamma_2^2\,\epsilon_{eff} - i\,\gamma_0^2\,\chi_{eff}(\theta)\right\}\, f(z) = 0 \ , \tag{73}$$

$$A_{har}\theta''(z) + \frac{P_l}{\lambda}\,\epsilon''_{eff}(\theta)(t_{22})|f|^2 = 0 \ , \tag{74}$$

subject to the boundary conditions

$$z = 0: \quad A_{har}\,\theta'(0) = B\,\theta(0) \ , \tag{75}$$

$$f'(0) + i\,\gamma_2\,\sqrt{\epsilon_{eff}}f(0) = 2\,i\,\gamma_2\sqrt{\epsilon_{eff}} \ , \tag{76}$$

$$z = 1: \quad \theta'(1) = 0 \ , \tag{77}$$

$$f'(1) - i\gamma_2\sqrt{\epsilon_{eff}}\,f(1) = 0 \ , \tag{78}$$

where B is the Biot number, or the nondimensional heat transfer coefficient from the effective material to the environment.

To characterize the solutions for $P > 0$, consider the bifurcation diagrams shown in Figure 8 for $\lambda = 2$, $\epsilon_1 = 1$, $\epsilon_2 = 4$, $B = 0.2$, $\gamma_2 = 1$, and $\beta = 3$. In these diagrams, also known as power response curves, we plot the average temperature $\overline{\theta}$ as a function of P for each solution at a given P. Solid portions of the curve correspond so stable solution branches, while dashed curves correspond to unstable branches. In Figure 8a, we consider the bifurcation diagrams for the periodic solutions, where the blue curves corresponds to the lower branch at $\gamma_o \approx 1.91$, while the red curve corresponds to the upper branch at $\gamma_o \approx 2.3$. Note that the form of these bifurcation diagrams corresponds to an S-shaped bifurcation diagram, which is typical in microwave heating applications [33, 49]. Thermal runaway is predicted by the first turning point, where the lowest stable branch containing $(P, \overline{\theta}) = (0, 0)$ becomes unstable at $(P, \overline{\theta}) = (P_c, T_c)$. We note that the lower value of γ_o becomes unstable at lower values of P compared to the larger values of γ_o for both the periodic and antiperiodic cases (as shown in Figure 8). Note that solutions corresponding to the upper branch for any of these solutions could result in loss factors which exceed our initial assumption that $\epsilon''_2 = O(\eta^2)$. Hence, in what follows, we focus only on the

Copyright © by SIAM. Unauthorized reproduction of this article is prohibited.

Downloaded 08/22/21 to 130.215.63.230. Redistribution subject to SIAM license or copyright; see https://epubs.siam.org/page/terms

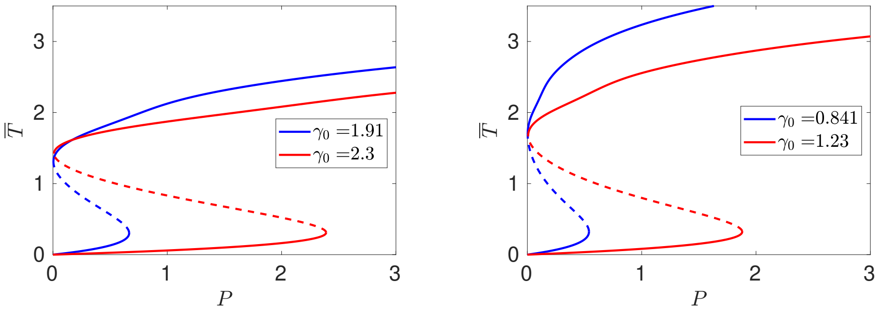

(a) (b)

Fig. 8. *Power response curves for $\lambda = 2$, $\gamma_2 = 1$, $\epsilon_1 = 1$, $\epsilon_2 = 4$, $B = 0.2$, and $\beta = 3$ for* (a) *the periodic modes and* (b) *the antiperiodic modes. (Figure in color online.)*

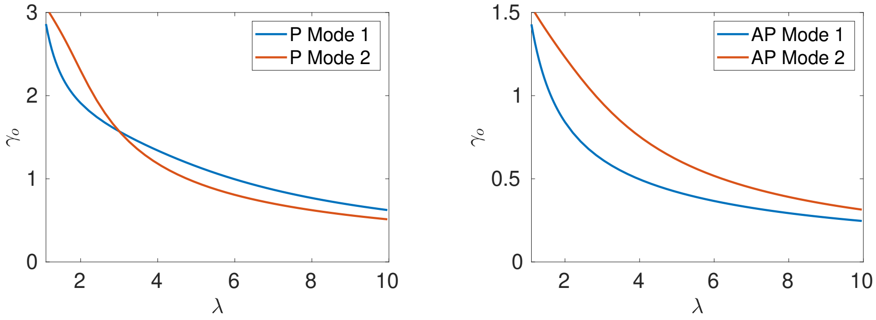

(a) (b)

Fig. 9. (a) *Dependence of γ_o on λ for the two periodic modes shown in Figure* 4a, $k = 0$. (b) *Dependence of γ_o on λ for the two antiperiodic modes shown in Figure* 4a, $\lambda\eta k = \pi$.

turning-point bifurcation between the lowest and middle branches of the bifurcation diagram.

To avoid thermal runaway, we need to understand how (P_c, T_c) depends on different volume fractions λ of the material. Changing this parameter changes the nature of the cell solution $U(\zeta)$, and we need to evaluate the corresponding γ_o for each of these cases. For clarity, we keep the remaining parameters fixed as in the cases shown in Figure 8. Figure 9 shows the behavior of γ_o for $1.1 < \lambda < 10$. Note that for the periodic case shown in Figure 9a that a degeneracy appears for $\lambda = 3$. In this case, $\gamma_o = \pi/2$, and closure on the cell problem occurs at $O(\eta)$ instead of $O(\eta^2)$. This case is beyond the scope of our current study.

In Figure 10a, we plot the critical power P_c at which the system becomes unstable for the two periodic modes. Note that for sufficiently large values of λ, the second periodic mode corresponding to $\gamma_o \approx 2.3$ at $\lambda = 2$ has a lower critical power than that for the first periodic mode. For the antiperiodic case, we see in Figure 10b that the first antiperiodic mode has a lower critical power than that for the second antiperiodic mode. In both of these cases, it is clear from Figure 11 that the temperature T_c at thermal runaway takes place over a relatively small range of values.

Copyright © by SIAM. Unauthorized reproduction of this article is prohibited.

Downloaded 08/22/21 to 130.215.63.230. Redistribution subject to SIAM license or copyright; see https://epubs.siam.org/page/terms

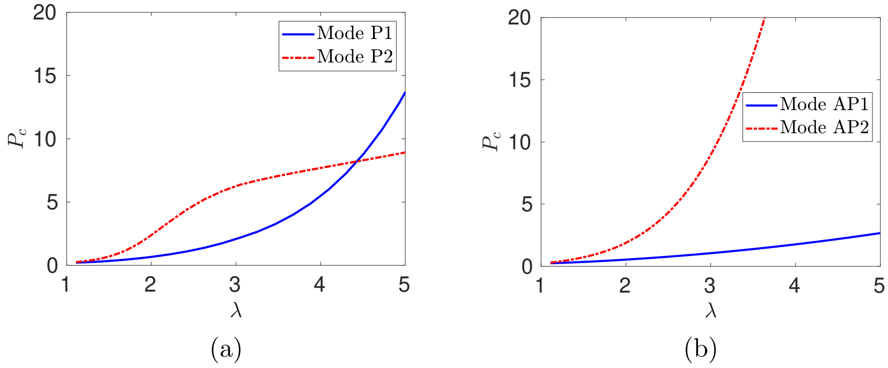

(a) (b)

FIG. 10. *Critical power P_c as a function of λ $\epsilon_1 = 1$, $\epsilon_2 = 4$, $B = 0.2$, and $\beta = 3$ for* (a) *the periodic modes, and* (b) *the antiperiodic modes.*

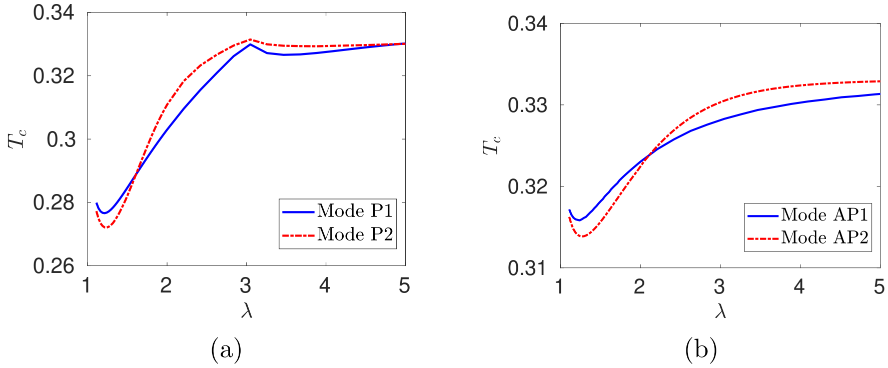

(a) (b)

FIG. 11. *Critical temperature T_c as a function of λ for $\epsilon_1 = 1$, $\epsilon_2 = 4$, $B = 0.2$, and $\beta = 3$ for* (a) *the periodic modes, and* (b) *the antiperiodic modes.*

6. Conclusions.

In this work, we consider the composite of two materials, one pure dielectric and the second a lossy dielectric. We determine the effective equations for wave propagation and energy transport when the loss factor in the lossy dielectric material is small. Since we study applications on beamed energy harnessing center on mm-wave frequencies, our analysis looks at the case when the wavelength of the applied field scales on the characteristic scale of the spatial periodicity of the microscale spatial pattern. We apply high-frequency homogenization for the electromagnetic problem and standard homogenization for the energy balance. The result is a coupled system of equation for the electric field amplitude and the temperature, where the parameters in these effective equations depend on different moments of the solutions to the cell problem. A 1D example is explored, where we validate this asymptotic solution computationally with an exact solution for the isothermal case. In this example, we also find that the presence of a nonzero loss factor eliminates band gaps, and better approximations to the wave propagation problem result when implementing the leading-order Bloch and attenuation parameters in the cell problem solution. Finally, for the 1D, we characterize how the volume fraction of the lossless material affects the transition to thermal runaway.

There are several repercussions as a result of this study. There are situations

Copyright © by SIAM. Unauthorized reproduction of this article is prohibited.

Downloaded 08/22/21 to 130.215.63.230. Redistribution subject to SIAM license or copyright; see https://epubs.siam.org/page/terms

where the cell problem solution is not unique. In the 1d example presented in section 4, this corresponds to the periodic solutions when $\lambda = 3$. The effective equations reduce to the same ones found by Craster, Kaplunov, and Pichugin [14], but this is one order of η larger than the loss factor. This implies for loss factors which depend on temperature, a temperature scale at which energy loss is significant scales on η in order for the asymptotic solution to be pertinent. For example, for an exponentially dependent loss factor discussed in section 4, this steady-state temperature scales on $\log 1/\eta$ for any $P > 0$. A separate local analysis near these specific spatial periods is needed to determine the steady-state behavior. Multimode interactions will lead to thermal runaway at lower power levels, provided that the net energy applied in the multimode case is larger than that for the monochromatic case. This is clear since the amplitude equation for the field strength of each mode is coupled only through the temperature. The presence of both modes in the material results in a larger effective power term in the energy equation, so thermal runaway takes place at lower temperatures compared to the monochromatic case. However, the critical temperature at which thermal runaway takes place depends on the relative amplitude of each mode.

In addition, one expects that for cases $\lambda_1 < \lambda < \lambda_2$, where λ_1, λ_2 are two spatial periods at which multiple solutions exist for the monochromatic cell problem, there is a value of λ such that the critical temperature at which thermal runaway takes place is minimized. This information can be useful depending on the choice of promoting or avoiding thermal runaway within the composite.

Importantly, this work points the way for developing a method to find effective equations for general periodic media. Provided that the cell problem can be solved computationally, then integrals of this solution provide the parameters to the effective media equations, along with the corresponding Bloch and attenuation parameters. The framework allows for the development of smart materials by manipulating the cell problem geometry to determine the macroscale response as described in Figure 3. Future work in this area will center in this area.

Appendix A. $O(\eta^{-1})$ analysis. Consider the cell problem for $\mathbf{E}^{(1)}$ with $\boldsymbol{\xi} \in \mathcal{V}$,

$$\nabla_\xi \cdot (\epsilon_j \mathbf{E}_j^{(1)}) = -\nabla_x \cdot (\epsilon_j \mathbf{E}_j^{(0)}) \ , \tag{79}$$

$$\begin{aligned} \nabla_\xi^2 \mathbf{E}_j^{(1)} + \gamma_0^2 \epsilon_j \mathbf{E}_j^{(1)} - \nabla_\xi(\nabla_\xi \cdot \mathbf{E}_j^{(1)}) &= -2(\nabla_x \cdot \nabla_\xi)\mathbf{E}_j^{(0)} - \gamma_1^2 \epsilon_j \mathbf{E}_j^{(0)} \\ &\quad + \nabla_\xi(\nabla_x \cdot \mathbf{E}_j^{(0)}) + \nabla_x(\nabla_\xi \cdot \mathbf{E}_j^{(0)}) \ , \end{aligned} \tag{80}$$

subject to the boundary conditions (21) for $\boldsymbol{\xi} \in \partial\Omega$ and appropriate periodic boundary conditions on $\mathcal{V}$ depending on the periodic/antiperiodic state of $\mathbf{E}^{(0)}$. Note that since $\mathbf{E}^{(0)} = f^{(0)}(\mathbf{x})\, \mathbf{U}^{(0)}(\boldsymbol{\xi}, \gamma_o)$, then

$$\nabla_x \cdot (\nabla_\xi \mathbf{E}^{(0)}) = \nabla_\xi \cdot (\nabla_x \mathbf{E}^{(0)}) = \left(\nabla_\xi \mathbf{U}^{(0)}\right)^T (\nabla_x f^{(0)}) \ .$$

Since the permittivity is constant, (79) becomes

$$\nabla_\xi \cdot \mathbf{E}^{(1)} = -\nabla_x \cdot \mathbf{E}^{(0)} = -(\nabla_x f^{(0)}) \cdot \mathbf{U}^{(0)} \ , \tag{81}$$

and along with $\nabla_\xi \cdot \mathbf{E}^{(0)} = 0$, this then gives us the following nonhomogeneous Helmholtz problem for $\mathbf{E}^{(1)}$:

$$\nabla_\xi^2 \mathbf{E}_j^{(1)} + \gamma_0^2 \epsilon_j \mathbf{E}_j^{(1)} = -2 \left(\nabla_\xi \mathbf{U}_j^{(0)}\right)^T (\nabla_x f^{(0)}) - \gamma_1^2 \epsilon_j f^{(0)}(\mathbf{x})\, \mathbf{U}_j^{(0)} \ . \tag{82}$$

Copyright © by SIAM. Unauthorized reproduction of this article is prohibited.

We require that the right-hand side of (82) must be orthogonal to $\mathbf{U}^{(0)}$ according to (22), and through this we find that

$$\begin{aligned}\int_{\mathcal{V}} \left(\mathbf{U}^{(0)}\right)^H \left\{\left(\nabla_\xi \mathbf{U}^{(0)}\right)^T \left(\nabla_x f^{(0)}\right)\right\} dV &= \int_{\mathcal{V}} \frac{1}{2}\left\{\nabla_\xi \left|\mathbf{U}^{(0)}\right|^2\right\} \cdot \left(\nabla_x f^{(0)}\right) dV \\ &= \frac{1}{2}\left\{\int_{\partial\mathcal{V}} |\mathbf{U}^{(0)}|^2 \,\mathbf{n}\, dS\right\} \cdot \left(\nabla_x f^{(0)}\right) = 0\end{aligned}$$

by periodicity of $\mathbf{U}^{(0)}$ on $\mathcal{V}$. Hence for compatability, $\gamma_1^2 = 0$.

Next, let us consider the two boundary conditions in (21) involving $\nabla_\xi \times \mathbf{E}^{(1)}$. First, consider

$$(\nabla_\xi \times \mathbf{E}_j^{(1)}) \cdot \mathbf{n}\Big|_1^2 = -\left(\nabla_x \times \mathbf{E}_j^{(0)}\right) \cdot \mathbf{n}\Big|_1^2, \qquad \boldsymbol{\xi} \in \partial\Omega\ . \tag{83}$$

Note that

$$\begin{aligned}\left(\nabla_x \times \mathbf{E}_j^{(0)}\right) \cdot \mathbf{n}\Big|_1^2 &= \left(f\nabla_x \times \mathbf{U}_j^{(0)} + \nabla_x f \times \mathbf{U}_j^{(0)}\right) \cdot \mathbf{n}\Big|_1^2 \\ &= \left(\nabla_x f \times \mathbf{U}_j^{(0)}\right) \cdot \mathbf{n}\Big|_1^2 \\ &= \left(\mathbf{U}_j^{(0)} \times \mathbf{n}\right)\Big|_1^2 \cdot \nabla_x f^{(0)} = 0\ ,\end{aligned}$$

since $\mathbf{U}^{(0)} \times \mathbf{n}$ is continuous across $\partial\Omega$. Hence $\left(\nabla_\xi \times \mathbf{E}_j^{(1)}\right) \cdot \mathbf{n}\Big|_1^2 = 0$ for $\xi \in \partial\Omega$.

Next, consider

$$\mathbf{n} \times \left(\nabla_\xi \times \mathbf{E}_j^{(1)}\right)\Big|_1^2 = -\,\mathbf{n} \times \left(\nabla_\xi \times \mathbf{E}_j^{(0)}\right)\Big|_1^2 . \tag{84}$$

From the form (18) for $\mathbf{E}^{(0)}$ we find that

$$-\,\mathbf{n} \times \left(\nabla_\xi \times \mathbf{E}_j^{(0)}\right)\Big|_1^2 = -\,\mathbf{n} \times (\nabla_x f \times \mathbf{U}^{(0)})\Big|_1^2 \tag{85}$$

since $\mathbf{U}^{(0)}$ is independent of $\mathbf{x}$.

Therefore, the reduced set of equations at $O(\eta^{-1})$ are

$$\nabla_\xi \cdot \mathbf{E}_j^{(1)} = -\nabla_x f \cdot \mathbf{U}_j^{(0)}, \quad \boldsymbol{\xi} \in \mathcal{V}\ , \tag{86}$$

$$\nabla_\xi^2 \mathbf{E}_j^{(1)} + \gamma_0^2 \epsilon_j \mathbf{E}_j^{(1)} = -2\left(\nabla_\xi \mathbf{U}_j^{(0)}\right)^T \nabla_x f^{(0)}\ , \tag{87}$$

with boundary conditions for $\boldsymbol{\xi} \in \partial\Omega$,

$$\mathbf{n} \cdot (\epsilon_j \mathbf{E}_j^{(1)})\Big|_1^2 = 0, \mathbf{n} \times \mathbf{E}_j^{(1)}\Big|_1^2 = \mathbf{0}, \tag{88}$$

$$\mathbf{n} \cdot (\nabla_\xi \times \mathbf{E}_j^{(1)})\Big|_1^2 = 0, \mathbf{n} \times (\nabla_\xi \times \mathbf{E}_j^{(1)})\Big|_1^2 = -\mathbf{n} \times \left(\nabla_x f \times \mathbf{U}_j^{(0)}\right)\Big|_1^2 \tag{89}$$

subject to periodicity conditions

$$\mathbf{E}^{(1)}\Big|_{\xi_i=1} = \mathbf{E}^{(1)}\Big|_{\xi_i=-1}, \qquad i = 1, 2, 3, \tag{90}$$

$$\frac{\partial \mathbf{E}^{(1)}}{\partial \xi_i}\bigg|_{\xi_i=1} = \frac{\partial \mathbf{E}^{(1)}}{\partial \xi_i}\bigg|_{\xi_i=-1}, \qquad i = 1, 2, 3. \tag{91}$$

Downloaded 08/22/21 to 130.215.63.230. Redistribution subject to SIAM license or copyright; see https://epubs.siam.org/page/terms

Copyright © by SIAM. Unauthorized reproduction of this article is prohibited.

Downloaded 08/22/21 to 130.215.63.230. Redistribution subject to SIAM license or copyright; see https://epubs.siam.org/page/terms

The general solution to the leading-order problem has the form

$$\mathbf{E}^{(1)} = f^{(1)}\mathbf{U}^{(0)} + \left[\underline{\underline{V}} - \mathbf{U}^{(0)}\boldsymbol{\xi}^T\right] \ , \tag{92}$$

where the column vectors of $\underline{\underline{V}}$ given by $\mathbf{v}_1$, $\mathbf{v}_2$, and $\mathbf{v}_2$ are nontriply periodic solutions of the leading-order cell problem. Next, we show (92) is a solution of the governing equations. Plugging (92) into (86) shows

$$\begin{aligned}\nabla_\xi \cdot \mathbf{E}^{(1)} &= f^{(1)}\nabla_\xi \cdot \mathbf{U}^{(0)} + \nabla_\xi \cdot \left[\left[\underline{\underline{V}} - \mathbf{U}^{(0)}\boldsymbol{\xi}^T\right]\left(\nabla_x f^{(0)}\right)\right] \\ &= 0 + \nabla_\xi \cdot \underline{\underline{V}}(\nabla_x f^{(0)}) - \nabla_\xi \cdot \left(\mathbf{U}^{(0)}\boldsymbol{\xi}^T\right)\left(\nabla_x f^{(0)}\right) \\ &= 0 - \mathbf{U}^{(0)\,T}(\nabla_x f^{(0)}) = -\nabla_x f^{(0)} \cdot \mathbf{U}^{(0)} \ .\end{aligned}$$

Therefore, we have shown that (92) solves Gauss' law at the first correction (86). Next, we do the same for the Helmholtz equation at the first correction. Plugging (92) into (87) shows

$$\begin{aligned}\nabla_\xi^2 \mathbf{E}_j^{(1)} + \gamma_0^2 \epsilon_j \mathbf{E}_j^{(1)} &= f^{(1)}\nabla_\xi^2 \mathbf{U}_j^{(0)} + \nabla_\xi^2 \left\{\left[\underline{\underline{V}} - \mathbf{U}^{(0)}\boldsymbol{\xi}^T\right]\left(\nabla_x f^{(0)}\right)\right\} \\ &\quad + \gamma_0^2 \epsilon_j \left\{f^{(1)}\mathbf{U}_j^{(0)} + \left[\underline{\underline{V}} - \mathbf{U}_j^{(0)}\boldsymbol{\xi}\right]\left(\nabla_x f^{(0)}\right)\right\} \\ &= \left\{\nabla_\xi^2 \underline{\underline{V}} + \gamma_o^2 \epsilon_j \underline{\underline{V}}\right\}(\nabla_x f^{(0)}) \\ &\qquad - \left\{\nabla_\xi^2 \left[\mathbf{U}_j^{(0)}\boldsymbol{\xi}^T\right] + \gamma_0^2 \epsilon_j \left[\mathbf{U}_j^{(0)}\boldsymbol{\xi}^T\right]\right\}\left(\nabla_x f^{(0)}\right) \\ &= -2\left(\nabla_\xi \mathbf{U}_j^{(0)}\right)^T \left(\nabla_x f^{(0)}\right) \ ,\end{aligned}$$

which is the right-hand side of the first correction Helmholtz equation.

Next, we show that the inhomogeneous jump condition (89) is also satisfied automatically by the bulk solution and thus causes no additional issue when it comes to closing the homogenized solution:

$$\begin{aligned}\mathbf{n} \times (\nabla_\xi \times \mathbf{E}_j^{(1)})\Big|_1^2 &= f^{(1)}\,\mathbf{n} \times (\nabla_\xi \times \mathbf{U}^{(0)})\Big|_1^2 \\ &\quad + \mathbf{n} \times \left(\nabla_\xi \times \left\{\left[\underline{\underline{V}} - \mathbf{U}^{(0)}\xi^T\right]\left(\nabla_x f^{(0)}\right)\right\}\right)\Big|_1^2 \end{aligned} \tag{93}$$

$$= 0 + \mathbf{n} \times \left[\nabla_\xi \times \underline{\underline{V}}\right]\Big|_1^2 \left(\nabla_x f^{(0)}\right) - \mathbf{n} \times \left(\nabla_\xi \times \left[\mathbf{U}^{(0)}\xi^T \nabla_x f^{(0)}\right]\right)\Big|_1^2 \tag{94}$$

$$\begin{aligned}&= 0 - \mathbf{n} \times \left\{\left[\xi^T \nabla_x f^{(0)}\right]\left(\nabla_\xi \times \mathbf{U}^{(0)}\right)\right\}\Big|_1^2 \\ &\quad + \mathbf{n} \times \left\{\nabla_\xi \left[\xi^T \nabla_x f^{(0)}\right] \times \mathbf{U}^{(0)}\right\}\Big|_1^2\end{aligned} \tag{95}$$

$$= 0 - \mathbf{n} \times \left(\nabla_x f^{(0)} \times \mathbf{U}^{(0)}\right)\Big|_1^2 . \tag{96}$$

This closes the first correction problem in terms of the leading-order solution $\mathbf{U}^{(0)}$.

Copyright © by SIAM. Unauthorized reproduction of this article is prohibited.

REFERENCES

[1] J. Aguilar-Garib, *Thermal microwave processing of materials*, in Advances in Induction and Microwave Heating of Mineral and Organic Materials, C. Grundas, ed., InTech Europe, Rijeka, Croatia, 2011, pp. 243–268.

[2] Y. Amirat and V. Shelukhin, *Homogenization of time harmonic Maxwell equations and the frequency dispersion effect*, J. Math. Pures Appl. (9), 95 (2011), pp. 420–443.

[3] S. Aravindan and K. Krishnamurthy, *Joining of ceramic composites by microwave heating*, Mater. Lett., 38 (1999), pp. 245–249.

[4] H. Banks, V. Bokil, D. Cioranescu, N. Gibson, G. Griso, and B. Miara, *Homogenization of periodically varying coefficients in electromagnetic materials*, J. Sci. Comput., 28 (2005), pp. 191–221.

[5] J. Binner, R. Morell, M. Porter, P. Kumi, and V. Yakovlev, *Simulation of temperature fields in microwave processing of SiCf/SiC composites*, in Proceedings of the 54th IMPI's Microwave Power Symposium, 2020, pp. 23–25 (virtual symposium).

[6] J. Binner, B. Vaidhyanathan, and D. Jaglin, *Microwave heated chemical vapour infiltration of SiC powder impregnated SiC fibre preforms*, Adv. Appl. Ceram., 112 (2013), pp. 235–241.

[7] Y. Bykov, K. Rybakov, and V. Semenov, *High-temperature microwave processing of materials*, J. Phys. D: Appl. Phys., 34 (2001), pp. R55–R75.

[8] L. Campañone and N. Zaritzky, *Mathematical analysis of microwave heating process*, J. Food Eng., 69 (2005), pp. 359–368.

[9] J. Carbonell, F. Cervera, J. Sánchez-Dehesa, J. Arriaga, L. Gumen, and A. Krokhin, *Homogenization of two-dimensional anisotropic dissipative photonic crystal*, Appl. Phys. Lett., 97 (2010), 231122.

[10] E. Cassan, J. Dellinger, X. le Roux, K. V. Do, F. de Fornel, and B. Cluzel, *Homogenization limit in a graded photonic crystal*, Phys. Rev. B, 88 (2013), 125138.

[11] S. Chandrasekaran, S. Ramanathan, and T. Basak, *Microwave materials processing – a review*, AlChE J., 58 (2012), pp. 330–363.

[12] S. Chandrasekaran, S. Ramanthan, and T. Basak, *Microwave food processing – A review*, Food Res. Int., 52 (2013), pp. 243–261.

[13] D. Clark and W. Sutton, *Microwave processing of materials*, Annu. Rev. Mater. Sci., 26 (1996), pp. 299–331.

[14] R. Craster, J. Kaplunov, and A. Pichugin, *High-frequency homogenization for periodic media*, Proc. R. Soc. Lond. Ser. A Math. Phys. Eng. Sci., 466 (2010), pp. 2341–2362.

[15] S. Das, A. Mukhopadhyay, S. Datta, and D. Basu, *Prospects of microwave processing: an overview*, Bull. Mater. Sci., 31 (2008), pp. 943–956.

[16] R. Depine, M. Martínez-Ricci, J. Monsoriu, E. Silvestre, and P. Andrés, *Zero permeability and zero permittivity band gaps in 1d metamaterial photonic crystals*, Phys. Lett. A, 364 (2008), pp. 352–355.

[17] D. Dincov, K. Parrott, and K. Pericleous, *Heat and mass transfer in two-phase porous materials under intensive microwave heating*, J. Food Eng., 65 (2004), pp. 403–412.

[18] U. Erle, P. Pescheck, and M. Lorence, *Development of Packaging and Products for Use in Microwave Ovens*, 2nd ed., Elsevier, 2020.

[19] J. Gaone, B. Tilley, and V. Yakovlev, *Electromagnetic heating control via high-frequency resonance of a triple-layer laminate*, J. Eng. Math., 114 (2019), pp. 65–86, https://doi.org/10.1007/s10665-018-9982-6.

[20] J. Gaone, B. Tilley, and V. Yakovlev, *Permittivity-based control of thermal runaway in a triple-layer laminate*, in Proceedings of the 2017 IEEE MTT-S International Microwave Symposium (IMS), 2017, pp. 459–462.

[21] M. Gawande, S. Shelke, R. Zboril, and R. Varma, *Microwave-assisted chemistry: synthetic applications fo rrapid assembly of nanomaterials and organics*, Acc. Chem. Res., 47 (2014), pp. 1338–1348.

[22] S. Guenneau, R. Craster, T. Antonakakis, K. Cherednichenko, and S. Cooper, *Homogenization techniques for periodic structures*, in Gratings: Theory and Numeric Applications, E. Popov, ed., Presses Universitaires de Provence (PUP), 2012, 11.

[23] P. Halevi, A. Krokhin, and J. Arriaga, *Photonic crystal optics and homogenization of 2D periodic composites*, Phys. Rev. Lett., 82 (1999), pp. 719–722.

[24] J. Jackson, *Classical Electrodynamics*, 3rd ed., John Wiley and Sons, New York, 1999.

[25] D. Jaglin, J. Binner, B. Vaidhyanathan, C. Prentice, B. Shatwell, and D. Grant, *Microwave heated chemical vapor infiltration: Densification mechanism of* sic_f/sic *composites*, J. American Ceramic Soc., 89 (2006), pp. 2710–2717.

Downloaded 08/22/21 to 130.215.63.230. Redistribution subject to SIAM license or copyright; see https://epubs.siam.org/page/terms

Copyright © by SIAM. Unauthorized reproduction of this article is prohibited.

Downloaded 08/22/21 to 130.215.63.230. Redistribution subject to SIAM license or copyright; see https://epubs.siam.org/page/terms

[26] G. Ji-Yong, C. Hong, L. Hong-Qiang, and Z. Ye-Wen, *Effective permittivity and permeability of one-dimensional dielectric photonic crystal within a band gap*, Chin. Phys. Soc., 17 (2008), pp. 2544–2552.

[27] J. Joannopoulos, S. Johnson, J. Winn, and R. Mead, *Photonic Crystals: Molding the Flow of Light*, 2nd ed., Princeton University Press, Princeton, NJ, 2008.

[28] L. Junyi and D. Balint, *An inverse method to determine the dispersion curves of periodic structures based on wave superposition*, J. Sound Vib., 350 (2015), pp. 41–72.

[29] E. Kiley, *Reduced-dimensional coupled electromagnetic, thermal, and mechanical models of microwave sintering*, Ph.D. Thesis, Worcester Polytechnic Institute, Worcester, MA, 2016.

[30] A. Kirchner, K. Busch, and C. Soukoulis, *Transport properties of random arrays of dielectric cylinders*, Phys. Rev. B, 57 (1998), pp. 277–288.

[31] W. Klinbun, K. Vafai, and P. Rattanadecho, *Electromagnetic field effects on transport through porous media*, Inter. J. Heat Mass Transfer, 55 (2012), pp. 325–335.

[32] S. Kochhar and A. Singh, *Developments in microwave processing of materials*, Asian J. Chem., 23 (2011), pp. 3307–3312.

[33] G. Kriegsmann, *Thermal runaway in microwave heated ceramics: A one-dimensional model*, J. Appl. Phys., 71 (1992), pp. 1960–1966.

[34] G. Kriegsmann, *Electromagnetic propagation in periodic porous structures*, Wave Motion, 36 (2002), pp. 457–472.

[35] G. Kriegsmann and B. Tilley, *Microwave heating of laminate panels*, J. Eng. Math., 44 (2002), pp. 173–198.

[36] A. Krokhin, P. Halevi, and J. Arriaga, *Long-wavelength limit (homogenization) for two-dimensional photonic crystals*, Phys. Rev. B, 65 (2002), 115208.

[37] K. Kumar and K. Reddy, *Thermal analysis of solar parabolic trough with porous disc receiver*, Appl. Energy, 86 (2009), pp. 1804–1812.

[38] P. Kumi, S. Martin, V. Yakovlev, M. Hilario, B. Hoff, and I. Rittersdorf, *Electromagnetic-thermal model of a millimeter-wave heat exchanger based on an AlN:Mo susceptor*, COMPEL – Int. J. Comp. Math. in Elec. Eng., 39 (2020), pp. 481–496.

[39] N. Leadbeater, *Microwave Heating as a Tool for Sustainable Chemistry*, in Sustainability: Contributions through Science and Technology, M. C. Cann, ed., CRC Press, Boca Raton, FL, 2010.

[40] C. Maniére, T. Zahrah, and E. Olevsky, *Inherent heating instability of direct microwave sintering process: Sample analysis for porous* $3Y$*-*ZRO_2, Scr. Mater., 128 (2017), pp. 49–52.

[41] P. Markos and C. Soukoulis, *Wave Propagation: From Electrons to Photonic Crystals and Left-handed Materials*, Princeton University Press, Princeton, NJ, 2008.

[42] F. Marra, J. Lyng, V. Romano, and B. McKenna, *Radio-frequency heating of foodstuff: solution and validation of a mathematical model*, J. Food Eng., 79 (2007), pp. 998–1006.

[43] F. Mavandadi and P. Lidström, *Microwave-assisted chemistry in drug discovery*, Curr. Top Med. Chem., 4 (2004), pp. 773–792.

[44] D. Maystre, *Getting effective permittivity and permeability equal to* -1 *in* 1*d dielectric photonic crystals*, J. Mod. Opt., 53 (2006), pp. 1901–1917.

[45] C. Mei and B. Vernescu, *Homogenization Methods for Multiscale Mechanics*, World Scientific, Singapore, 2010.

[46] R. Menezes, P. Souto, and R. Kiminami, *Microwave fast sintering of ceramic materials*, in Sintering of Ceramics – New Emerging Techniques, A. Lakshmanan, ed., InTech, Rijeka, Croatia, 2012.

[47] R. Mishra and A. Sharma, *Microwave-material interaction phenomena: Heating mechanisms, challenges and opportunities in material processing*, Compos. Part A Appl. Sci. Manuf., 81 (2016), pp. 78–97.

[48] A. Mohekar, J. Gaone, B. Tilley, and V. Yakovelev, *Multiphysics simulation of temperature profiles in a triple-layer model of a microwave heat exchanger*, in Proceedings of the 2018 IEEE MTT-S International Microwave Symposium (IMS), 2018, pp. 1389–1392.

[49] J. Pelesko and G. Kriegsmann, *Microwave heating of ceramic composites*, IMA J. Appl. Math., 64 (2000), pp. 34–50.

[50] M. Regler, K. Knoerzer, and H. Schubert, *The Microwave Processing of Foods*, 2nd ed., Woodhead Publishing, Sawston, UK, 2016.

[51] A. Sihvola, *Electromagnetic Mixing Formulas and Applications*, Electromagnetic Waves 47, The Institution of Electrical Engineers, London, 1999.

[52] A. Sihvola, *Homogenization principles and effect of mixing on dielectric behavior*, Photonics Nanostructures: Fundam. Appl., 11 (2013), pp. 364–373.

[53] S. Singh, D. Gupra, V. Jain, and A. Sharma, *Microwave processing and applications of*

Copyright © by SIAM. Unauthorized reproduction of this article is prohibited.

manufacturing industry: a review, Mater. Manuf. Process., 30 (2015), pp. 1–29.

[54] D. Sjöberg, C. Engström, G. Kristensson, D. Wall, and N. Wellander, *A Floquet–Bloch decomposition of Maxwell's equations applied to homogenization*, Multiscale Model. Simul., 4 (2005), pp. 149–171, https://doi.org/10.1137/040607034.

[55] K. Sopian, M. Alghoul, E. Alfegi, M. Sulaiman, and E. Musa, *Evaluation of thermal efficiency of double-pass solar collector with porous-nonporous media*, Renew. Energy, 34 (2009), pp. 640–645.

[56] B. Tilley and G. Kriegsmann, *Microwave-enhanced vapor infiltration: A sharp interface model*, J. Eng. Math., 41 (2001), pp. 33–54.

[57] E. Tuncer, *Dielectric mixtures - importance and theoretical approaches*, IEEE Electr. Insul. Mag., 29 (2013), pp. 49–58.

[58] V. Veselago, *The electrodynamics of substances with simultaneously negative values of ϵ and μ*, Sov. Phys. Usp., 10 (1968), pp. 509–514.

[59] A. Vinogradov and A. Merzlikin, *On the problem of homogenization one-dimensional systems*, J. Exper. Theor. Phys., 94 (2002), pp. 482–488.

[60] N. Wellander and G. Kristensson, *Homogenization of the Maxwell equations at fixed frequency*, SIAM J. Appl. Math., 64 (2003), pp. 170–195, https://doi.org/10.1137/S0036139902403366.

[61] M. Willert-Porada, *Advances in Microwave and Radio Frequency Proceedings*, Springer, Berlin, Heidelberg, 2006.

[62] X. Wu, *Experimental and Theoretical Study of Microwave Heating of Thermal Runaway Materials*, Ph.D. thesis, Virginia Polytechnic Institute, Blacksburg, VA, 2002.

[63] X. Wu, J. Thomas, and W. Davis, *Control of thermal runaway in microwave resonant cavities*, J. Appl. Phys., 92 (2002), pp. 3374–3380.

[64] V. Yakovlev, S. Allan, M. Fall, and H. Shulman, *Computational study of thermal runaway in microwave processing of zirconia*, in Microwave and RF Power Applications, J. Tao, ed., Cépaduès Éditions, 2011, pp. 303–306.

[65] L. Zhou, V. Puri, R. Anantheswaran, and G. Yeh, *Finite element modeling of heat and mass transfer in food materials during microwave heating – Model development and validation*, J. Food Eng., 25 (1995), pp. 509–529.

Downloaded 08/22/21 to 130.215.63.230. Redistribution subject to SIAM license or copyright; see https://epubs.siam.org/page/terms

Copyright © by SIAM. Unauthorized reproduction of this article is prohibited.